International Journal of Non–Linear Mechanics 187 (2026) 105364

Contents lists available at ScienceDirect

International Journal of Non-Linear Mechanics

journal homepage: www.elsevier.com/locate/nlm

Bandgap manipulation through a bi-stable inertially amplified strongly nonlinear periodic chain

A. Bhattacharyya *,[1], S. Adhikari

James Watt School of Engineering, The University of Glasgow, Glasgow G12 8QQ, UK

ARTICLE INFO

Keywords:
Nonlinear elastic metamaterial
Bi-stable snap-through element
Perturbation methods
Bloch's theorem
Harmonic balance method
Inverse method

ABSTRACT

Metamaterials and periodic structures can exhibit geometric or kinematic nonlinearities that generate non-integrable, non-polynomial force expressions. Such systems, including tensegrity structures, origami-inspired lattices, and bi-stable mechanical systems, resist standard analytical techniques for predicting amplitude-dependent wave propagation and bandgap behavior. Hence, ALIGN (Amplitude-Locked, Inverse method-Guided, multi-harmonic Nonlinear framework), a novel semi-analytical methodology is proposed that addresses three fundamental challenges: evaluating Fourier projections when forcing terms contain algebraic singularities (square roots, denominators near kinematic limits), setting multi-harmonic initial conditions that achieve prescribed steady-state amplitudes in time-domain validation, and tracking dispersion branches through frequency degeneracies where continuation algorithms typically fail. The framework employs time-domain collocation with complex-step differentiation for robust Jacobian assembly, iterative Root Mean Square (RMS) amplitude targeting for systematic inverse-method validation, and Modal Assurance Criterion-based feature matching on high-dimensional harmonic coefficient vectors for branch continuity. Demonstrated on a bi-stable-inertial periodic chain with coupled horizontal-vertical dynamics, the methodology successfully bridges weakly and strongly nonlinear regimes, identifies critical mass-ratio thresholds defining dynamic instability boundaries consistent across both regimes, validates amplitude-dependent dispersion predictions with significant accuracy across parameter space, and achieves at least 10 times computational speedup compared to direct time-domain simulation while still successfully predicting dispersion characteristics for finite real-world periodic models. This work provides a systematic and generalizable pathway for analyzing discrete periodic systems with geometric nonlinearities applicable to structures where forces are expressible as algebraic functions, enabling rapid parametric design space exploration for vibration isolation, wave filtering, and adaptive mechanical metamaterial applications.

1. Introduction

Periodic media and mechanical metamaterials have attracted considerable attention for wave control, enabling phenomena such as band gaps, directionality, and amplitude-dependent dispersion [1–7]. Classical foundations in wave propagation in periodic structures [8,9] underpin modern phononic and acoustic metamaterials where dispersion can be engineered via geometry, internal resonators, and material heterogeneity [4–6]. Active and adaptive designs have been developed to manipulate acoustic and elastic waves [10]. Nonlinear effects, including bistability and large deformations, allow tunable band structures and dynamic behaviors unavailable in linear lattices [2,11,12]. These advances in engineered dispersion have broad implications for vibration isolation, noise filtering, and energy harvesting applications [13].

Recent studies have focused on novel periodic lattices incorporating complex internal mechanisms. In particular, inertial amplification, where a levered mass increases the effective inertia, has been shown to widen low-frequency band gaps [14–16]. This concept has even been used in seismic isolation design, where optimally designed nonlinear inertial absorbers can enhance structural resilience [17]. Similarly, chains of bi-stable (snap-through) elements have been explored for bandgap generation via nonlinear buckling [18]. Elastic and solitary wave propagation has been thoroughly studied, both analytically and numerically, in a periodic chain consisting of bi-stable elastic elements [19]. Related work on one-dimensional granular and tensegrity lattices demonstrates asymmetric and amplitude-dependent wave phenomena [20–22]. Meanwhile, designs with attached resonators or

* Corresponding author.
E-mail address: 2756762b@student.gla.ac.uk (A. Bhattacharyya).
[1] Doctoral researcher.

https://doi.org/10.1016/j.ijnonlinmec.2026.105364
Received 9 February 2026; Received in revised form 25 March 2026; Accepted 25 March 2026
Available online 26 March 2026

auxiliary masses have been proposed to improve vibration attenuation and bandgap control [23]. Together, these efforts highlight the potential for bandgap engineering through tailored nonlinearity and resonance [4,7].

On the theoretical side, various analytical and numerical methods have been applied to nonlinear lattice waves. Perturbation and multiple-scale techniques have been used to derive dispersion relations for weakly nonlinear chains [24–29]. Floquet–Bloch analysis provides a rigorous framework for dispersion in periodic media [8,9], while spectral and finite-element approaches have also been applied to investigate band structures in complex metamaterials [30–34]. Recent work has even incorporated data-driven modeling to capture nonlinear wave behavior in structured media [35]. For strongly nonlinear responses, generalized harmonic balance (HB) and related reduced-order approaches (e.g., nonlinear normal modes) offer systematic routes to compute amplitude-dependent dispersion and internal resonances [27,29,36,37]. A spectral submanifold (SSM) approach has also been used for model reduction and forced-response calculation in high-dimensional nonlinear systems [38,39]. While these existing tools are powerful, two practical limitations still recur in nonlinear periodic media with geometric/constraint nonlinearities: (a) the nonlinearity is often non-polynomial/non-integrable (e.g., square root terms) so closed-form Fourier projections become cumbersome or unavailable, and (b) dispersion extraction over the Brillouin zone is prone to branch switching and degeneracies, especially when multiple periodic solutions coexist or when modal content redistributes strongly with μ and amplitude.

Existing literature and reviews cover many metamaterial concepts but leave certain gaps in this context. For example, surveys of elastic metamaterials emphasize local resonators and nonlinearity [2,5,6,13] but do not consider a lattice with combined inertial amplification and bi-stable elements. Prior studies have examined inertial amplification in isolation [14,40] and bi-stable chains separately [18,19], but the dispersion of a hybrid system with both features is largely unexplored. Also, rigorous analytical and numerical studies of periodic chains comprising of linear oscillators coupled to perpendicularly oscillating bi-stable oscillators do not exist in the current literature. This gap motivates a comprehensive dispersion and bandgap analysis through our proposed framework and its demonstration on a system exhibiting the full range of analytical and computational challenges. Hence, we propose this work to address the limitations discussed through an Amplitude-Locked, Inverse method-Guided, multi-harmonic Nonlinear framework (ALIGN). The central advancement over standard continuation-based periodic-orbit workflows is that ALIGN is formulated specifically for nonlinear Bloch waves. It enforces Bloch quasi-periodicity directly at the unit-cell residual level, handles non-integrable geometric nonlinearities via time-collocation harmonic balance with complex-step differentiation (avoiding analytic Fourier integrals), and performs global branch stitching across wavenumber μ using MAC-based feature matching on high-dimensional harmonic coefficient vectors. In addition, ALIGN couples the semi-analytical dispersion computation to an amplitude-locked time-domain validation stage (inverse method, IM), where multi-harmonic initial conditions are constructed from HB coefficients and the finite-chain response is iteratively locked to a prescribed RMS amplitude. This combination targets a key gap in much of the nonlinear dispersion literature, which is a systematic, amplitude-conditioned verification pipeline for strongly nonlinear Bloch wave predictions.

The second novelty lies in the hybrid dynamical system considered. Here, we propose and analyze a 3 DOF bi-stable-inertial unit cell and its periodic repetition, producing coupled horizontal-vertical dynamics with non-integrable geometric force terms and amplitude-dependent dispersion. To the best of the authors' knowledge, a periodic lattice that combines inertial amplification with bi-stable geometric nonlinearity in this configuration has not previously been analyzed in the context of nonlinear Bloch dispersion and bandgap evolution.

In summary, the specific contributions are:

- A new bi-stable-inertial periodic lattice model with coupled horizontal-vertical dynamics as a testbed for nonlinear bandgap engineering beyond local-resonator-only and bi-stable-only chains.
- The ALIGN workflow for computing amplitude-dependent nonlinear Bloch dispersion in systems with non-polynomial/non-integrable geometric nonlinearities, using multi-harmonic HB with time-collocation and complex-step Jacobians.
- Robust dispersion-branch tracking across the Brillouin zone via MAC-based matching of harmonic coefficient vectors, enabling consistent stitching through near degeneracies and strong modal redistribution.
- Systematic time-domain verification via an amplitude-locked inverse method (IM) using multi-harmonic initial conditions extracted from HB, thereby quantitatively linking semi-analytical dispersion predictions to finite-chain simulations.

To address the gap discussed, we analyze in a unified way the dispersion and bandgap properties of the proposed periodic lattice in both the weakly and strongly nonlinear regimes. First, in Section 2, we lay out a motivation behind proposing a bi-stable-inertial 3 degree of freedom (DOF) model with coupled horizontal-vertical dynamics as a repeating unit for building periodic nonlinear structures or in general nonlinear metamaterials by studying its behavior in the time-domain and phase space. After we build a periodic chain by repeating this proposed 3 DOF model, at first, we assume small displacements from a global energy minimum and perform an asymptotic expansion of the equations of motion, which yields a hierarchy of linearized problems. The leading order system is treated with Bloch's theorem, leading to a generalized eigenvalue problem for the linear dispersion relation, from which we compute dispersion curves and band diagrams under varying design parameters. At higher order, the same asymptotic framework provides analytic corrections to the frequencies and clarifies how the bi-stable geometry and inertial amplification jointly influence the band structure. To capture large-amplitude motions beyond the reach of perturbation theory, we then retain the exact nonlinear equations and apply a generalized multi-harmonic harmonic balance (HB) method coupled with Galerkin projection and complex step differentiation. The resulting nonlinear algebraic system is solved using Newton–Raphson iteration, producing amplitude-dependent dispersion curves for the full, non-integrable nonlinearity. Taken together, these steps provide a single, consistent pathway from linear to strongly nonlinear behavior, allowing us to systematically chart how band gaps evolve with amplitude and design parameters rather than relying solely on a small-amplitude approximation [29,36,37].

For direct time-domain verifications, we embed these semi-analytical tools within a full amplitude-locked direct time-domain simulation workflow and validate the resulting dispersion predictions via direct time-domain simulations of large, finite chains (inverse method or "IM" validation). For each Bloch wavenumber and branch, we construct multi-harmonic initial conditions from the harmonic-balance coefficients, lock the time-domain response to a prescribed root mean square (RMS) amplitude, and extract operating frequencies using band-pass/Hilbert-based estimators with zero-crossing fallbacks. This validation step is carried out systematically in Section 7, following the development of the generalized framework in Section 3, the problem-specific formulation of the bi-stable–inertial unit cell in Section 4, and the weakly nonlinear perturbation analysis and band-structure exploration in Section 5. Section 6 then deploys the generalized harmonic balance method to compute dispersion curves in the strongly nonlinear regime and to compare them directly with the perturbation-based predictions, while Section 7 uses the IM numerical time-domain simulations to assess agreement, probe the robustness of the band gaps, and highlight regimes where localization, strong modal interactions, and possible routes to chaos emerge [41,42]. Although a detailed dynamical-systems analysis of these complex responses lies beyond

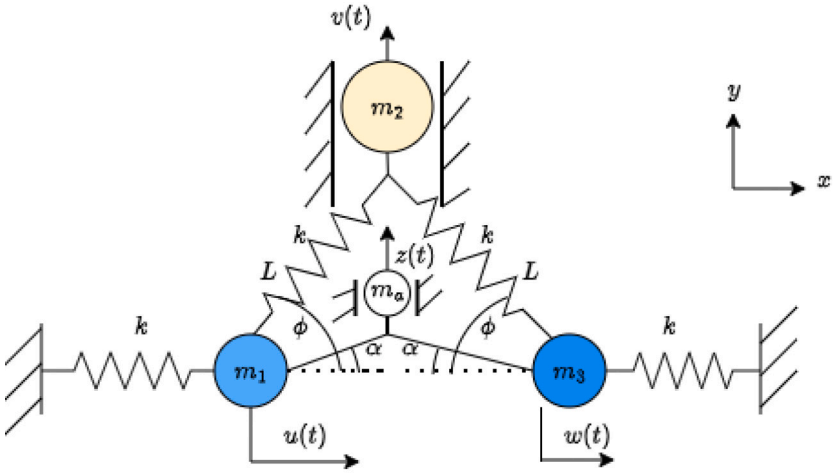

Fig. 1. The 3 degree of freedom bi-stable-inertial model fixed at both ends, where $u(t)$, $w(t)$ represent the horizontal degrees of freedom of masses m_1 and m_3 respectively, $v(t)$ represents the vertical degree of freedom of the bi-stable mass m_2, $z(t)$ denotes the inertially coupled vertical degree of freedom of the inertial amplifier mass m_a, k denotes the linear stiffness co-efficients of all the springs, L denotes the natural length of the springs in the initial undeformed configuration, ϕ denotes the angle of inclination of the inclined linear springs with the horizontal axis in the initial undeformed configuration, α denotes the angle of inclination of the rigid links with the horizontal axis in the initial undeformed configuration.

the scope of the introduction, this section-wise pipeline underscores that the proposed methodology not only fills the identified gap in the literature but also provides multiple, mutually consistent lenses such as perturbation theory, harmonic balance, and time-domain simulation, through which the behavior of the hybrid bi-stable–inertial lattice can be understood and critically assessed.

Nomenclature

See Table 1.

2. A bi-stable-inertial unit cell underpinning nonlinear metamaterials

2.1. The mechanical model

We choose a 3 degree of freedom (DOF) model which consists of a bi-stable mass (m_2) constrained to move in the vertical direction coupled by inclined linear springs with two linear spring-mass oscillators having degrees of freedom in the horizontal direction (m_1 and m_3). The horizontally moving masses are fixed to rigid supports via linear horizontal springs. In addition, the masses m_1 and m_3 are coupled via rigid links to an inertial amplifier mass m_a also constrained to move in the vertical direction. The angle of inclination of the linear springs with the horizontal axis in the initial undeformed configuration is denoted by ϕ and the angle of inclination of the rigid links with the horizontal axis in the initial undeformed configuration is denoted by α. It is assumed that $\phi > \alpha$. The inertial amplifier is also constrained to move in the vertical direction. The displacement of the two linear oscillators are denoted by u and w in the horizontal direction and the displacement of the bi-stable mass is denoted by v in the vertical direction. The displacement of the inertial amplifier mass denoted by z. The natural length of the springs are denoted by L. The linear stiffness co-efficients of the inclined and horizontal springs are taken as k. A schematic diagram of the model is shown in Fig. 1. This specific model is chosen because of its rich dynamical configuration capable of showing both bi-stability and inertial amplification with coupled horizontal-vertical dynamics and intrawell and interwell oscillations of the mass m_2. We hence perform a thorough dynamic analysis of the system behavior in the phase space before proposing this model as a constituent repeating unit cell for enhanced bandgap manipulation in nonlinear metamaterials.

2.2. Dynamic analysis in the phase plane

2.2.1. Equations of motion and non-dimensionalization

The displacements u and w are measured in the positive x direction from the reference points in the initial unstressed configuration as shown in Fig. 1, where all the springs are unstressed and are in their natural undeformed length L. The displacement v is measured in the positive y direction and the reference $v = 0$ is taken at the axis of the horizontal linear springs which is shown by dotted horizontal lines in Fig. 1. So, in the initial unstressed equilibrium configuration which is shown in Fig. 1, $v = L\sin\phi$. The equations of motion for the model can be derived from its Lagrangian and are obtained as:

$$m_1\ddot{u} + ku - k(L\cos\phi - u)\left(1 - \frac{L}{\sqrt{(L\cos\phi - u)^2 + v^2}}\right) + F\cos\alpha = 0 \quad (1)$$

$$m_2\ddot{v} + kv\left(2 - \frac{L}{\sqrt{(L\cos\phi - u)^2 + v^2}} - \frac{L}{\sqrt{(L\cos\phi + w)^2 + v^2}}\right) = 0 \quad (2)$$

$$m_3\ddot{w} + kw + k(L\cos\phi + w)\left(1 - \frac{L}{\sqrt{(L\cos\phi + w)^2 + v^2}}\right) - F\cos\alpha = 0 \quad (3)$$

The force exerted by the rigid links on the masses m_1 and m_3 is denoted by F. From system kinematics, the displacement of the inertial amplifier mass $z(t)$ can be written in terms of the displacements of the two oscillators $u(t)$, $w(t)$ and angle α as

$$z = \frac{w - u}{2}\cot\alpha \quad (4)$$

Differentiating Eq. (4) twice with respect to time gives

$$\ddot{z} = \frac{\ddot{w} - \ddot{u}}{2}\cot\alpha \quad (5)$$

Force balance on the inertial amplifier gives

$$m_a\ddot{z} = 2F\sin\alpha \quad (6)$$

With these relations (Eqs. (5), (6)), Eqs. (1), (2), (3) can be rewritten as

$$m_1\ddot{u} + ku - k(L\cos\phi - u)\left(1 - \frac{L}{\sqrt{(L\cos\phi - u)^2 + v^2}}\right) + \frac{m_a(\ddot{w} - \ddot{u})\cos^2\alpha}{4\sin^2\alpha} = 0 \quad (7)$$

$$m_2\ddot{v} + kv\left(2 - \frac{L}{\sqrt{(L\cos\phi - u)^2 + v^2}} - \frac{L}{\sqrt{(L\cos\phi + w)^2 + v^2}}\right) = 0 \quad (8)$$

Table 1
Notations and abbreviations used in the manuscript.

Symbol	Description	Units
Dimensional variables and parameters		
t	Time	s
$u(t)$	Horizontal displacement of mass m_1	m
$w(t)$	Horizontal displacement of mass m_3	m
$v(t)$	Vertical displacement of bi-stable mass m_2	m
$z(t)$	Vertical displacement of inertial-amplifier mass m_a	m
m_1	Left horizontal oscillator mass	kg
m_2	Bi-stable (vertical) oscillator mass	kg
m_3	Right horizontal oscillator mass	kg
m_a	Inertial-amplifier mass	kg
k	Linear spring stiffness (inclined and horizontal springs)	N/m
L	Natural length of inclined springs (undeformed)	m
F	Force transmitted through rigid links to m_1 and m_3	N
ϕ	Initial inclination angle of inclined springs to horizontal	rad
α	Initial inclination angle of rigid links to horizontal	rad
ω_n	Reference angular frequency, $\omega_n = \sqrt{k/m_1}$	rad/s
Nondimensional variables (using $\tau = \omega_n t$ and scaling by L)		
τ	Nondimensional time, $\tau = \omega_n t$	–
$(\cdot)'$	Derivative with respect to τ	–
$\dot{(\cdot)}$	Derivative with respect to t	–
η	Nondimensional horizontal displacement, $\eta = u/L$	–
ψ	Nondimensional horizontal displacement, $\psi = w/L$	–
ξ	Nondimensional vertical displacement, $\xi = v/L$	–
r_1	Mass ratio, $r_1 = m_2/m_1$	–
r_2	Mass ratio, $r_2 = m_3/m_1$	–
r_a	Mass ratio, $r_a = m_a/m_1$	–
χ_a	Inertial amplification factor, $\chi_a = \frac{r_a \cos^2\alpha}{4\sin^2\alpha}$	–
F_η	Nondimensional restoring force associated with η	–
F_ξ	Nondimensional restoring force associated with ξ	–
F_ψ	Nondimensional restoring force associated with ψ	–
U	Nondimensional potential energy, $U(\eta, \xi, \psi)$	–
ω	Nondimensional wave frequency (scaled by ω_1)	–
T_0	Nondimensional period, $T_0 = 2\pi/\omega$	–
ω_ξ	Linearized natural frequency of ξ about a stable well (as defined in text)	–
Periodic chain, Bloch quantities, and indices		
n	Unit cell index in an infinite periodic chain	–
j	Unit cell index in a finite chain (IM validation)	–
j_0	Reference unit-cell index (center/excitation reference)	–
N	Number of unit cells in the finite chain (e.g., 300 in IM)	–
N_{exc}	Half-width (in cells) of the spatial excitation window (if used)	–
d	Number of DOFs per unit cell (here $d = 3$)	–
μ	Non-dimensional Bloch wavenumber/phase advance per cell (first Brillouin zone)	–
$Re(\cdot)$	Real part	–
$Im(\cdot)$	Imaginary part	–
Weakly nonlinear perturbation notation		
ϵ	Small parameter governing perturbation expansion (set by IC amplitude)	–
δ_n	Small deviation of η_n from equilibrium, $\eta_n = 0 + \delta_n$	–
λ_n	Small deviation of ψ_n from equilibrium, $\psi_n = 0 + \lambda_n$	–
ζ_n	Small deviation of ξ_n from equilibrium, $\xi_n = \sin\varphi + \zeta_n$	–
$(\cdot)^{(0)}$	Leading-order ($\mathcal{O}(\epsilon)$) term	–
$(\cdot)^{(1)}$	Next-order ($\mathcal{O}(\epsilon^2)$) correction	–
ω_0	Leading-order frequency in $\omega = \omega_0 + \epsilon\omega_1 + \mathcal{O}(\epsilon^2)$	–
ω_1	First correction to ω in the perturbation expansion (context-dependent)	–
A_0	Leading-order wave amplitude parameter used in perturbation correction	–
HB/ALIGN and IM validation quantities		
N_h	Number of harmonics retained in the HB expansion	–
N_t	Number of time-collocation points per period in HB	–
θ_k	Collocation phase point, $\theta_k = 2\pi k/N_t$	rad
m	Harmonic index, $m = 1, \ldots, N_h$	–

(*continued on next page*)

$$m_3\ddot{w} + kw + k(L\cos\phi + w)\left(1 - \frac{L}{\sqrt{(L\cos\phi + w)^2 + v^2}}\right) - \frac{m_a(\ddot{w} - \ddot{u})\cos^2\alpha}{4\sin^2\alpha} = 0 \tag{9}$$

The characteristic length for non-dimensionalization is taken to be the natural length of the springs L. The non-dimensional time is taken as $\tau = \omega_n t$, where $\omega_n = \sqrt{\frac{k}{m_1}}$. The mass ratios are taken as $\frac{m_2}{m_1} = r_1$, $\frac{m_3}{m_1} = r_2$ and $\frac{m_a}{m_1} = r_a$. The non-dimensional displacements are obtained as $\eta = \frac{u}{L}$, $\xi = \frac{v}{L}$ and $\psi = \frac{w}{L}$. With this, the non-dimensional equations of motion are obtained as

$$\eta'' + \eta - (\cos\phi - \eta)\left(1 - \frac{1}{\sqrt{(\cos\phi - \eta)^2 + \xi^2}}\right) + \frac{r_a(\psi'' - \eta'')\cos^2\alpha}{4\sin^2\alpha} = 0 \tag{10}$$

$$r_1\xi'' + \xi\left(2 - \frac{1}{\sqrt{(\cos\phi - \eta)^2 + \xi^2}} - \frac{1}{\sqrt{(\cos\phi + \psi)^2 + \xi^2}}\right) = 0 \tag{11}$$

Table 1 (*continued*).

A	Input amplitude scaling parameter used in HB displacement ansatz	–
$\mathbf{c}_m$	Cosine harmonic coefficient vector of the displacement (HB)	–
$\mathbf{s}_m$	Sine harmonic coefficient vector of the displacement (HB)	–
$\mathbf{X}$	HB unknown vector (e.g., $\omega, \{\mathbf{c}_m, \mathbf{s}_m\}$ with gauge conditions)	–
$\mathbf{r}(\theta_k; \mathbf{X}, \mu)$	Time-collocation residual at phase θ_k	–
$\mathbf{R}(\mathbf{X}; \mu; A)$	Harmonic-balance algebraic residual after projection	–
MAC	Modal Assurance Criterion used for branch tracking across μ	–
RMS	Root-mean-square amplitude metric used for amplitude targeting in IM	–
IC	Initial condition	–
HB	Harmonic balance	–
IM	Inverse method (time-domain validation)	–
DOF	Degree of freedom	–
NNM	Nonlinear normal mode	–
IBZ	Irreducible Brillouin zone/first Brillouin zone (as used in text)	–

$$r_2\psi'' + \psi + (\cos\phi + \psi)\left(1 - \frac{1}{\sqrt{(\cos\phi+\psi)^2 + \xi^2}}\right) - \frac{r_a(\psi'' - \eta'')\cos^2\alpha}{4\sin^2\alpha} = 0 \tag{12}$$

where prime denotes differentiation with respect to the non-dimensional time τ.

This specific model with a bi-stable mass coupled to two orthogonally moving linear oscillators is considered because of its unique coupled vertical-horizontal dynamics. Previous studies like [43] have considered either the bi-stable mass in isolation as a single DOF system or a periodic chain of single DOF bi-stable masses coupled to each other by horizontal linear springs acting as force transfer elements [19] capable of exhibiting only horizontal dynamics.

2.2.2. Phase plane behavior

We investigate how the bi-stable mass (m_2) behaves when coupled to masses m_1 and m_3 in its phase plane (displacement ξ vs. velocity ξ') by direct numerical simulations of the governing non-dimensional equations of motion (Eqs. (10)–(12)) and plot the Poincare sections for different values of the system parameters.

The nonlinear elastic restoring forces acting on masses m_1, m_2, m_3 are given by

$$\begin{aligned} F_\eta &= -\eta + (\cos\phi - \eta)\left(1 - \frac{1}{\sqrt{(\cos\phi-\eta)^2+\xi^2}}\right) \\ F_\xi &= -\xi\left(2 - \frac{1}{\sqrt{(\cos\phi-\eta)^2+\xi^2}} - \frac{1}{\sqrt{(\cos\phi+\psi)^2+\xi^2}}\right) \\ F_\psi &= -\psi - (\cos\phi + \psi)\left(1 - \frac{1}{\sqrt{(\cos\phi+\psi)^2+\xi^2}}\right) \end{aligned} \tag{13}$$

where F_η, F_ξ and F_ψ are the forces acting on the masses m_1, m_2 and m_3 respectively in their non-dimensional forms. These are forces which have been derived from a potential function. So, we can say that when these forces collectively become zero, those corresponding displacements refer to a stationary (local minima/local maxima) point of the potential energy of the system as a whole. On considering the potential function of the system in the non-dimensional form as $U = U(\eta, \xi, \psi)$ and setting the partial derivatives with respect to the three degrees of freedom η, ξ, ψ to zero like

$$\frac{\partial U}{\partial \eta} = \frac{\partial U}{\partial \xi} = \frac{\partial U}{\partial \psi} = 0 \tag{14}$$

We obtain two energy minima of the system at $(\eta, \xi, \psi) = (0, \pm\sin\phi, 0)$, which is quite evident from the bi-stable nature of the oscillator m_2. Had the bi-stable oscillator been connected to rigid supports instead of masses m_1 and m_3, it would have two stable centers at $\xi = \pm\sin\phi$ and one unstable saddle at $\xi = 0$ taking into account that the same scheme of non-dimensionalization has been used.

It is well-known from existing literature [42] that forced bi-stable oscillators or double-well oscillators exhibit chaotic strange attractor motion or transient chaos for large enough amplitude of the forcing when it undergoes interwell oscillations or snap-through motion. The corresponding Poincare map generates a scattered, non-repeating set of points which fall on a fractal set which can be interpreted as a cross-section for chaotic strange attractors for sustained chaos, and two sets of closed Poincare points for transient chaos where the motion ultimately settles into small periodic oscillations in one of the energy wells. In our chosen 3 DOF model, in contrast to a single DOF bi-stable mass connected to rigid supports, we have the bi-stable mass coupled to two orthogonal degrees of freedom. We examine the phase-plane behavior of this system and subsequent Poincare maps by taking projections of the six-dimensional phase space on two-dimensional planes, where for any particular mass, the projection is taken on the plane defined by its corresponding displacement and velocity. For examining the phase-plane behavior, we use direct numerical simulations with the fourth-order Runge–Kutta method (ode45 in MATLAB). For initial conditions of the system as for now, we keep the initial states of masses m_1 and m_3 at zero and apply an initial state of displacement and velocity on the bi-stable mass m_2 in order to study its rich dynamics specifically. Since we are interested in manipulating the dispersion characteristics of 'free' wave propagation using this model as a repeating block, we do not apply any kind of forcing in our system and study the phase behavior evolving solely due to the initial conditions imposed.

We use two sets of initial conditions for the double-well mass m_2 in the non-dimensional form, one keeping the mass m_2 close to its unstable equilibrium position or saddle at $\xi = 0$ and one keeping the mass m_2 close to one of its stable equilibrium positions at $\xi = \sin\phi$. Since we do not apply any driving force in our system and let it evolve freely, it is practically difficult to define a Poincare section even in a two-dimensional projection of the six-dimensional phase space. So, we obtain the Poincare map for m_2 by plotting the points $\xi(\tau)$ and $\xi'(\tau)$ whenever τ is an integer multiple of $\frac{2\pi}{\omega_\xi}$, where we define ω_ξ as the non-dimensional linearized natural frequency of m_2 which can be easily obtained by assuming small perturbations from the stable equilibrium point of m_2 at $\xi = \sin\phi$ and performing a Taylor series expansion. As will be shown later in Eq. (23), this non-dimensional linearized natural frequency is obtained as $\omega_\xi = \sqrt{\frac{2\sin^2\phi}{r_1}}$. For each set of initial conditions, we use three sets of values of the mass ratios r_1, r_2, r_a, keeping $r_2 = 1$ to maintain spatial symmetry and hence avoid the issues of non-similarity and energy-dependence of the modal curves as much as possible.

Figs. 2 and 3 show the time-domain response, phase orbit and Poincare maps for the bi-stable mass m_2 in our chosen 3 DOF model for two sets of initial conditions of m_2, keeping the initial states of masses m_1 and m_3 at zero.

As we can see from Fig. 2, when we impose an initial displacement condition on m_2 close to its unstable equilibrium point or saddle at $\xi = 0$, the time-domain response consists of several snap-through motions where the mass m_2 crosses the energy hump at $\xi = 0$ repeatedly and undergoes interwell oscillations between the two energy wells at $\xi = \pm\sin\phi = \pm 0.6$. The phase orbit shows a tangled set of pairs of

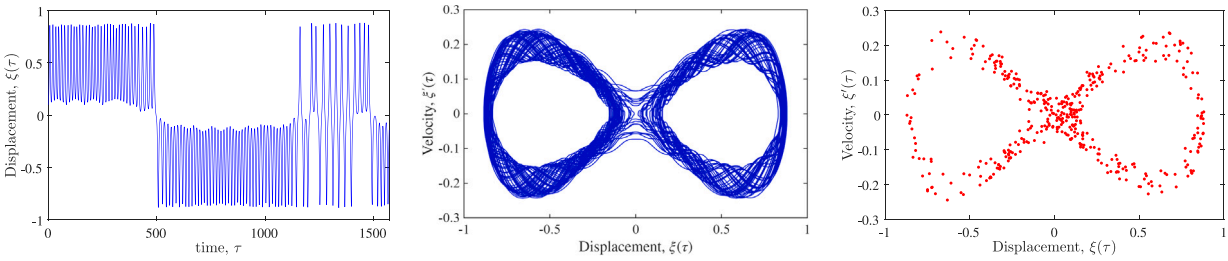

(a) Time-domain response for $r_1 = 1$, $r_2 = 1$, $r_a = 0.5$ (b) Phase orbit for $r_1 = 1$, $r_2 = 1$, $r_a = 0.5$ (c) Poincare map for $r_1 = 1$, $r_2 = 1$, $r_a = 0.5$

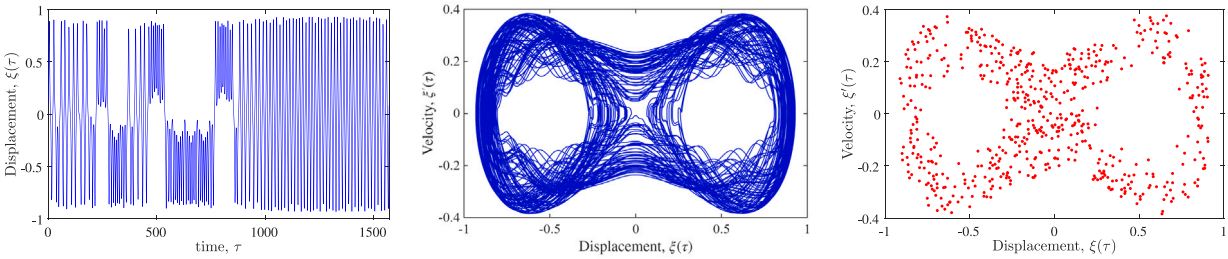

(d) Time-domain response for $r_1 = 0.5$, $r_2 = 1$, $r_a = 0.5$ (e) Phase orbit for $r_1 = 0.5$, $r_2 = 1$, $r_a = 0.5$ (f) Poincare map for $r_1 = 0.5$, $r_2 = 1$, $r_a = 0.5$

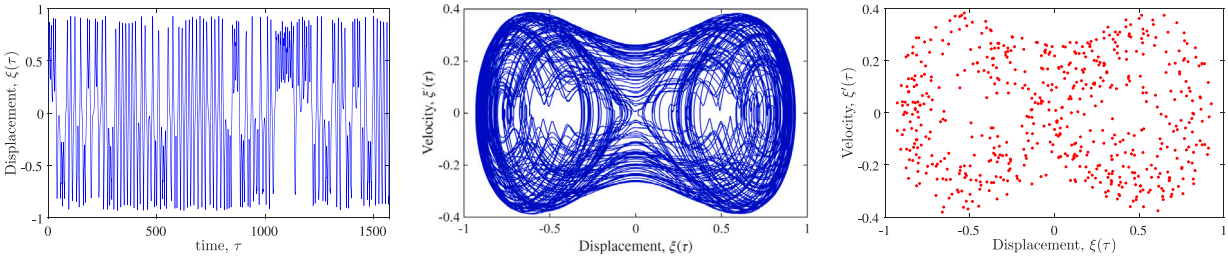

(g) Time-domain response for $r_1 = 0.5$, $r_2 = 1$, $r_a = 0.3$ (h) Phase orbit for $r_1 = 0.5$, $r_2 = 1$, $r_a = 0.3$ (i) Poincare map for $r_1 = 0.5$, $r_2 = 1$, $r_a = 0.3$

Fig. 2. Time-domain response, phase orbit and Poincare maps for the bi-stable mass m_2 in our chosen 3 DOF model for initial conditions, $\xi(0) = 0.1$, $\xi'(0) = 0$, keeping the initial states of masses m_1 and m_3 to be zero. Angles of inclination in the initial unstressed equilibrium configuration are taken as $\sin\phi = 0.6$ and $\sin\alpha = 0.5$.

homoclinic orbits due to multiple crossings of the energy hump for our chosen time window. The tangled appearance arises as an artifact of taking a two-dimensional projection of our six-dimensional phase space which is typical of systems with more than two variables in the phase space. The Poincare section instead of falling on a fractal set as was in the case of a single DOF forced double-well oscillator [42], shows multiple sets of pairs of homoclinic orbits. Although the time-domain motion is aperiodic and suggests the possibility of transient chaos, the Poincare section does not indicate the existence of a strange attractor, so we can draw a qualitative assumption that there can be transient chaos in our 3 DOF model before the mass m_2 settles down in one of its two potential wells or to periodic oscillations with large amplitudes around its saddle at $\xi = 0$. We also notice that the time-domain and phase-plane behavior is sensitively dependent on the combination of the mass ratios r_1, r_2, r_a while keeping the initial conditions and other parameters fixed. As we go from Figs. 2(a) and 2(b) to Figs. 2(d) and 2(e), keeping r_2 and r_a fixed, as $r_1 = \frac{m_2}{m_1}$ is decreased from 1 to 0.5, the mass m_2 undergoes more intrawell oscillations around the stable equilibrium points at $\xi = \pm\sin\phi$ and periodic oscillations with larger amplitudes around the saddle at $\xi = 0$ in addition to interwell oscillations. We notice this same trend as we go from Figs. 2(d) and 2(e) to Figs. 2(g) and 2(h), keeping r_1 and r_2 fixed, and decreasing $r_a = \frac{m_a}{m_1}$ from 0.5 to 0.3, i.e. more intrawell oscillations around $\xi = \pm\sin\phi$ and periodic oscillations with large amplitudes around the saddle at $\xi = 0$ of the mass m_2. This dependence of intrawell oscillations and large-amplitude periodic motions on the mass ratios sets a useful motivation for using this model as a repeating unit for manipulating wave dispersion characteristics by varying the mass ratios in discrete nonlinear periodic structures or in general nonlinear metamaterials.

Fig. 3 shows the time-domain response, phase-plane behavior and Poincare section for the mass m_2 in our 3 DOF model, when we impose an initial displacement condition on m_2 sufficiently close to its stable equilibrium position at $\sin\phi = 0.6$ and keep the initial states of masses m_1 and m_3 at zero. Quite expectedly, the mass m_2 for this initial condition, remains close to its initial stable configuration and performs intrawell oscillations within the energy well at $\sin\phi = 0.6$ as can be seen from Fig. 3. For our chosen time window, we get repeated closed orbits each corresponding to one complete oscillation in the energy well. Although we see a dependence of the dynamic behavior on the mass ratios in this case as well. As we keep r_2 fixed and decrease both r_1 and r_a, we get more cycles of oscillations in the energy well. However, the mass m_2 for this initial condition close to its stable equilibrium

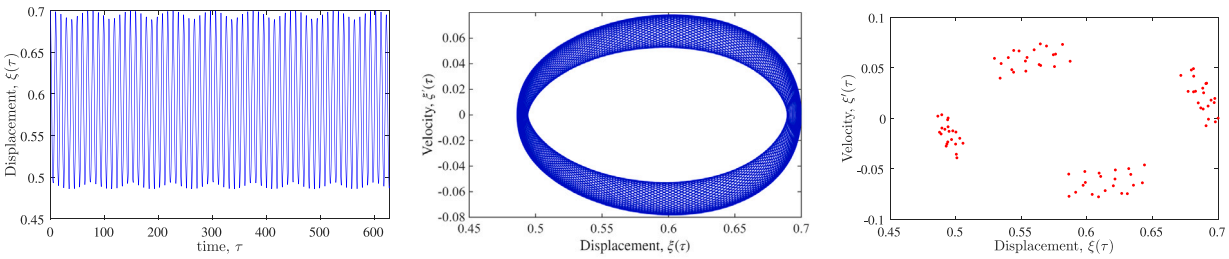

(a) Time-domain response for $r_1 = 1$, $r_2 = 1$, $r_a = 0.5$ (b) Phase orbit for $r_1 = 1$, $r_2 = 1$, $r_a = 0.5$ (c) Poincare map for $r_1 = 1$, $r_2 = 1$, $r_a = 0.5$

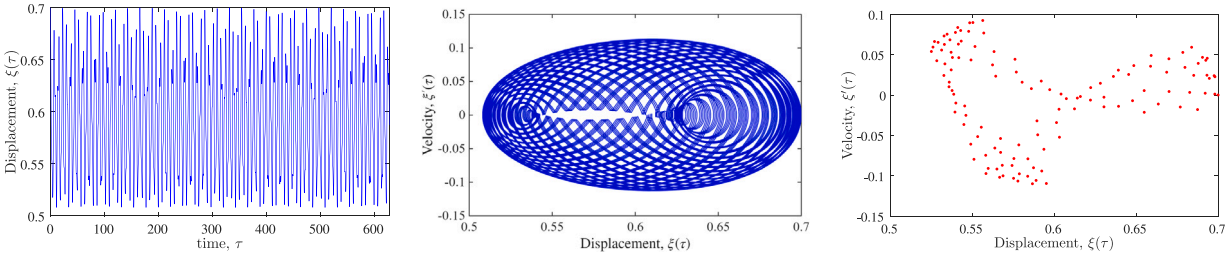

(d) Time-domain response for $r_1 = 0.5$, $r_2 = 1$, $r_a = 0.3$ (e) Phase orbit for $r_1 = 0.5$, $r_2 = 1$, $r_a = 0.3$ (f) Poincare map for $r_1 = 0.5$, $r_2 = 1$, $r_a = 0.3$

Fig. 3. Time-domain response, phase orbit and Poincare maps for the bi-stable mass m_2 in our chosen 3 DOF model for initial conditions, $\xi(0) = 0.7$, $\xi'(0) = 0$, keeping the initial states of masses m_1 and m_3 to be zero. Angles of inclination in the initial unstressed equilibrium configuration are taken as $\sin\phi = 0.6$ and $\sin\alpha = 0.5$.

position, even if coupled to orthogonally moving masses m_1 and m_3, never crosses the saddle or the energy hump at $\xi = 0$, and stays in its potential well at $\xi = \sin\phi$. This becomes useful if we want to study the behavior of a periodic structure composed of this 3 DOF model as a repeating unit, close to its global energy minima by using standard analytical techniques like perturbation methods or asymptotic analysis.

Overall, we can say that the double-well or bi-stable oscillator m_2 in spite of being coupled to two orthogonal degrees of freedom, preserves its rich and complex nonlinear dynamical behavior to a significant extent close to its stable/unstable equilibrium points and this sets our motivation to use this 3 DOF model as a repeating unit for manipulating wave propagation properties in nonlinear periodic structures or fancily called nonlinear metamaterials.

3. A generalized, consolidated framework for discrete nonlinear periodic structures

The major challenge faced while performing the dynamic analysis of general strongly nonlinear discrete periodic systems is usually the lack of a generalized analytical framework which arises due to the coupled ordinary differential-difference equations with non-integrable, non-polynomial forcing terms. The next difficulty arises due to the sensitive dependence of the response of strongly nonlinear systems on the initial conditions which complexifies the direct time-domain validation of the analytical/semi-analytical results across a wide range of input amplitudes. To capture the response of dynamic systems in their inherently strongly nonlinear regime, we often need to use more than a single harmonic term for the displacement approximation in the steady state. This makes the direct time-domain validation complicated in the sense that what initial conditions we should impose on the system as a whole so that traveling waves can sustain in the system and the output amplitude envelope matches with the target amplitudes desired to achieve from those sets of initial conditions. To overcome these challenges, we develop an Amplitude-Locked, Inverse method-Guided, multi-harmonic Nonlinear framework (ALIGN), a framework that computes amplitude-dependent dispersion via multi-harmonic harmonic balance (HB) and validates it by inverse method (IM) simulations whose input envelopes are locked to the HB solution through a root mean square (RMS) amplitude target.

3.1. Notation and unit-cell modeling

We consider a one-dimensional (1D) periodic chain obtained by the repetition of an identical unit cell with d generalized coordinates (DOFs) $\mathbf{u}_n(t) \in \mathbb{R}^d$ denoting the vector of degrees of freedom (DOFs), where $n \in \mathbb{Z}$ indexes the cell and t is time. The equations of motion for an undamped, unforced system are written in standard form as

$$\mathbf{M}\,\ddot{\mathbf{u}}_n(t) + \mathbf{f}\big(\mathbf{u}_{n-1}(t),\, \mathbf{u}_n(t),\, \mathbf{u}_{n+1}(t)\big) \;=\; \mathbf{0} \tag{15}$$

where $\mathbf{M} \in \mathbb{R}^{d\times d}$ is the (constant, symmetric positive definite) mass matrix of the unit cell and $\mathbf{f}(\cdot)$ collects all internal forces, including linear couplings to the nearest neighbors and any nonlinear terms internal to the cell. We allow $\mathbf{f}$ to be non-integrable (e.g., algebraic and non-polynomial, possibly non-separable in the DOFs), as often arises in geometric or constraint-based nonlinearities.

Spatial periodicity is treated via the Bloch (Floquet) phase $\mu \in [0, \pi]$ (first Brillouin zone). For any field $\mathbf{u}_n$, Bloch quasi-periodicity implies $\mathbf{u}_{n\pm1}(t) = \mathbf{u}_n(t)\, e^{\pm i\mu}$ in the frequency-domain picture; in the time-domain implementation we enforce the same coupling at the level of unit-cell residuals.

3.2. Linear baseline and weakly nonlinear perturbations

Linearization of (15) around the trivial equilibrium yields the generalized eigenvalue problem

$$\big(\mathbf{K}(\mu) - \omega^2\,\mathbf{M}\big)\,\boldsymbol{\phi}(\mu) \;=\; \mathbf{0} \tag{16}$$

where $\mathbf{K}(\mu)$ is the Bloch-reduced stiffness matrix of size $d \times d$ and $\omega(\mu)$ are the linear dispersion branches. In the weakly nonlinear regime one may introduce a perturbation parameter ϵ multiplying the nonlinear

part of $\mathbf{f}$ and apply an asymptotic expansion (e.g., multiple scales or averaging) to derive amplitude-dependent corrections to $\omega(\mu)$, modal interaction conditions (internal resonances), and slowly-varying envelope equations. This perturbative picture provides a baseline and a consistency check for the fully nonlinear computations that follow.

3.3. Generalized harmonic balance for strongly nonlinear responses

When nonlinearities are strong and/or non-polynomial, closed-form Fourier coefficients of $\mathbf{f}$ are typically unavailable. We therefore adopt a time-domain collocation (or quadrature) variant of harmonic balance (HB). We seek time-periodic, Bloch-consistent solutions [11] with fundamental frequency $\omega > 0$ and N_h harmonics:

$$\mathbf{u}_n(t) \approx A \sum_{m=1}^{N_h} \Big[\mathbf{c}_m \cos\big(m(\mu n - \omega t)\big) + \mathbf{s}_m \sin\big(m(\mu n - \omega t)\big) \Big] \tag{17}$$

where $\mathbf{c}_m, \mathbf{s}_m \in \mathbb{R}^d$ are harmonic coefficient vectors, μ and ω are wavenumber and frequency respectively as used in their standard notations. A is an input amplitude parameter. To remove the trivial amplitude/phase indeterminacy we impose a gauge on the first harmonic (e.g., fix one component of $\mathbf{c}_1$ and leave the corresponding $\mathbf{s}_1$ free).

Let $\theta_k = 2\pi k/N_t$ $(k = 1, \dots, N_t)$ be a uniform grid over one period, where N_t is the chosen number of points in the time-domain. Define the stacked vector of unknowns

$$\mathbf{X} = \big(\omega,\ \mathbf{c}_1, \mathbf{s}_1, \dots, \mathbf{c}_{N_h}, \mathbf{s}_{N_h}\big)$$

with the chosen gauge enforced explicitly. For each θ_k we evaluate the kinematic fields implied by (17) and assemble the unit-cell residual

$$\mathbf{r}(\theta_k; \mathbf{X}, \mu) = \mathbf{M}\,\ddot{\mathbf{u}}_0(\theta_k) + \mathbf{f}\Big(\mathbf{u}_{-1}(\theta_k),\ \mathbf{u}_0(\theta_k),\ \mathbf{u}_{+1}(\theta_k)\Big)$$

where $\mathbf{u}_{\pm 1}(\theta_k) = \mathbf{u}_0(\theta_k) e^{\pm i\mu}$ (or, equivalently, the neighbor contributions are assembled using the Bloch phase). The HB residual is the time-projection of $\mathbf{r}$ onto the trigonometric basis, which we compute by numerical quadrature (e.g., trapezoidal rule over the N_t points). This yields a nonlinear system $\mathbf{R}(\mathbf{X}; \mu; A) = \mathbf{0}$ of size $2N_h d$ (because of imposing the gauge and fixing the values of μ and A as inputs), which we solve by Newton's method with a backtracking line-search. The Jacobian $\partial\mathbf{R}/\partial\mathbf{X}$ is formed either analytically or robustly via complex-step differentiation, which is accurate and avoids step-size tuning issues.

Continuation in μ and branch stitching: For each μ we initialize Newton using the corresponding linear eigen pair of Eq. (16) (or the converged solution at the previous μ). To track branches consistently through crossings and near-degeneracies, we compare multi-harmonic feature vectors (all $\mathbf{c}_m, \mathbf{s}_m$ across the d DOFs) between successive μ-points using a modal assurance criterion (MAC), optionally regularized by a weak frequency-proximity weight. This provides a minimal, model-agnostic way to prevent branch swapping.

3.4. Inverse (time-domain) method for independent validation

To validate the semi-analytical HB dispersion, we simulate a long but finite chain in the time domain and extract the dominant frequency for each target (μ, branch). A localized, Bloch-consistent initial condition (IC) is synthesized by superposing the N_h harmonics from the HB coefficients,

$$u_j^{(q)}(0) \approx A \sum_{m=1}^{N_h} \big(c_m^{(q)} \cos(m\mu(j - j_0)) + s_m^{(q)} \sin(m\mu(j - j_0)) \big) \tag{18}$$

for each DOF $q = 1, \dots, d$ over an excitation window centered at j_0. The index of the unit cells is represented by j and j_0 is the reference unit cell index. This excitation window can span the entire length of the finite version (say N) of the periodic structure or can extend from $j_0 - N_{exc}$ to $j_0 + N_{exc}$, where N_{exc} is the number of cells chosen for initial spatial displacement excitation. We keep the initial velocities to be zero intentionally. Since we are considering more than one harmonic in the HB approximation, we need to set a target amplitude based on a rough approximation of the HB coefficients which we want the DOFs to achieve at steady state in the time-domain. We choose the root mean square (RMS) amplitude of the different HB coefficients multiplied by the input amplitude parameter A to be this target amplitude. We then propagate the full nonlinear dynamics over a time interval that excludes reflections/boundary effects (absorbing or damping layers can be used at the boundaries) and spatially demodulate the response using $e^{-i\mu(j-j_0)}$ over a small measurement window to obtain a complex scalar trace $y^{(q)}(t)$ per DOF. A band-pass + Hilbert transform estimator around the HB ω (or a zero-crossing fallback) returns a measured frequency; if multiple DOFs are available, we retain the candidate closest to the HB target. This procedure (often called an "inverse method" in this context) provides branch-wise frequency curves from direct simulations, suitable for cross-checking the HB dispersion in both weakly and strongly nonlinear regimes.

3.5. Handling non-integrable, non-polynomial nonlinearities

A distinguishing feature of many metamaterial cells is the presence of non-integrable nonlinearities, for example algebraic, non-separable terms induced by geometric constraints or kinematic closures. Typical components of $\mathbf{f}$ may look like

$$g(\eta, \xi) = (\alpha \pm \eta)\left(1 - \frac{1}{\sqrt{(\alpha \pm \eta)^2 + \xi^2 + \delta^2}}\right)$$

where η, ξ are cell DOFs, α collects geometric parameters, and $\delta > 0$ is a small analytic regularizer that prevents singular denominators near kinematic limits. Such non-polynomial terms are generally not amenable to closed-form Fourier integrals. The HB strategy above circumvents this by:

- evaluating $\mathbf{f}$ pointwise in time on the collocation grid, so no harmonic integrals of $g(\cdot)$ are needed;
- using sufficiently fine N_t (e.g., $N_t \geq 512\, N_h$) to accurately resolve sharp features from the algebraic nonlinearity;
- employing complex-step differentiation to assemble a stable Jacobian for Newton, avoiding finite-difference cancellation when g is steep;
- applying a light harmonic taper in the branch-stitching features (e.g., weights $\propto 1/\sqrt{m}$) so high harmonics stabilize rather than destabilize continuation;
- enforcing a simple gauge (e.g., fix one component of $\mathbf{c}_1$) to remove global phase/scale ambiguity.

In practice this combination has two benefits: (a) it keeps the method generic, no model-specific Fourier algebra is required and (b) it remains applicable in the strongly nonlinear regime, where high harmonics are essential.

3.6. From weak to strong nonlinearity: one workflow

Bringing the elements together, a practical workflow that applies across discrete nonlinear periodic structures is:

- Linear baseline: compute $\omega(\mu)$ from Eq. (16) for intuition and seeding.
- HB sweep in μ: for each μ, solve $\mathbf{R}(\mathbf{X}; \mu) = \mathbf{0}$ with $N_h \geq 1$, increase N_h as nonlinearity strengthens. Use MAC-based feature matching for branch assignment and a simple reseeding guard (fall back to linear seed if the converged ω collapses well below the linear ω).
- IM validation: build multi-harmonic, Bloch-consistent initial conditions (ICs) from the HB coefficients, set a target amplitude for the DOFs to achieve in the time-domain by using RMS approximation, demodulate, estimate frequency, and compare against HB.

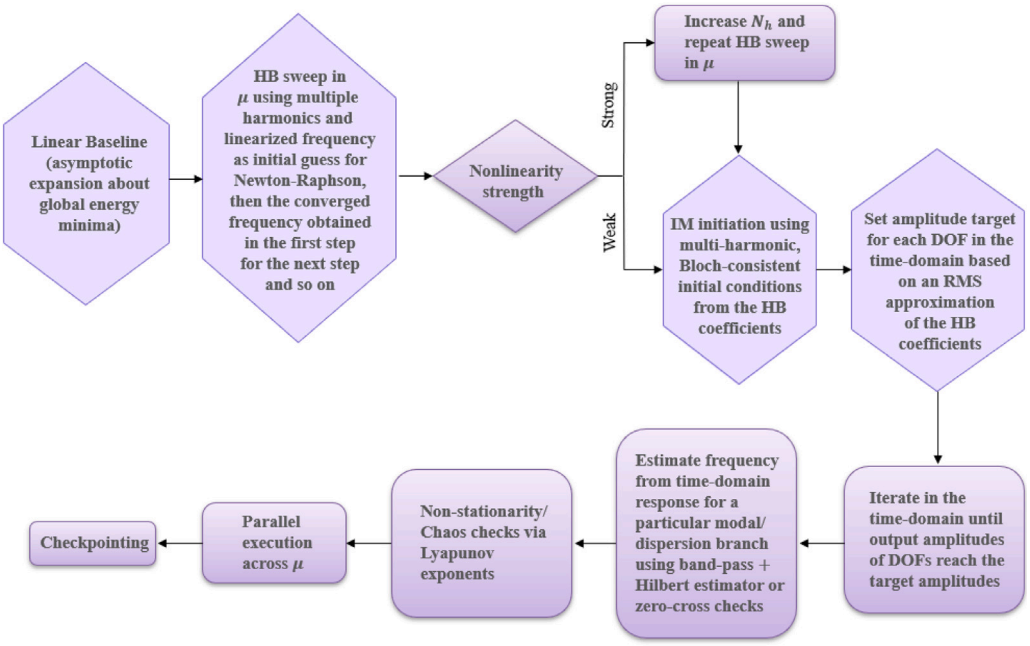

Fig. 4. ALIGN workflow: multi-harmonic Harmonic Balance (HB) with global branch stitching and amplitude-conditioned seeding, followed by Inverse Method (IM) validation using Root Mean Square (RMS) targeting and Hilbert-based frequency estimation. Stored coefficients $\{c_{mj}, s_{mj}\}$ enable multi-harmonic Initial Conditions (ICs) for the IM stage.

- Nonstationarity and chaos checks: when needed, examine spectrograms, return maps, or Lyapunov exponents on the time traces to flag modulation/chaos. HB captures periodic responses and departures warn of quasiperiodicity or chaos.

The residual assembly in the HB step is parallel in μ and within a μ in the collocation points θ_k. For large sweeps, parallel execution across μ values and checkpointing the arrays $\{\omega(\mu), \mathbf{c}_m(\mu), \mathbf{s}_m(\mu)\}$ facilitates robust runs on HPC systems. The IM validation is likewise parallel across μ and across branches/initializations.

The formulation summarized in Fig. 4 is deliberately model-agnostic. It covers lattice cells with any number of DOFs, linear and nonlinear nearest-neighbor couplings, and both integrable (polynomial) and non-integrable (algebraic/geometry-induced) nonlinearities. It provides a single pipeline spanning weak to strong nonlinearity, from semi-analytical (HB) dispersion to independent time-domain validation (IM), and is intended to set up the problem-specific details that follow in Section 4.

4. Specific problem formulation: An inertially amplified strongly nonlinear periodic chain

To arrive at a periodic one-dimensional chain, we consider an array of N unit cells where each repeating unit cell is our previously considered 3 degree of freedom model discussed in Section 2. The periodic chain is constructed by repeating the 3 DOF model and linking via horizontal linear coupling springs between m_1 and m_3 of adjacent unit cells in one dimension i.e. the horizontal direction. This appears to be a fairly intricate example of a discrete nonlinear periodic structure which can be tuned to design nonlinear metamaterials. A schematic diagram of the periodic chain constructed with the repeating unit cell is shown in Fig. 5. The non-dimensional equations of motion of the nth unit cell, Eqs. (19)–(21) are obtained easily using the non-dimensional equations of motion of the 3 DOF model (Eqs. (10), (11), (12)) as reference.

$$\eta_n'' + (\eta_n - \psi_{n-1}) - (\cos\phi - \eta_n)\left(1 - \frac{1}{\sqrt{(\cos\phi - \eta_n)^2 + \xi_n^2}}\right) + \frac{r_a(\psi_n'' - \eta_n'')\cos^2\alpha}{4\sin^2\alpha} = 0 \tag{19}$$

$$r_1\xi_n'' + \xi_n\left(2 - \frac{1}{\sqrt{(\cos\phi - \eta_n)^2 + \xi_n^2}} - \frac{1}{\sqrt{(\cos\phi + \psi_n)^2 + \xi_n^2}}\right) = 0 \tag{20}$$

$$r_2\psi_n'' + (\psi_n - \eta_{n+1}) + (\cos\phi + \psi_n)\left(1 - \frac{1}{\sqrt{(\cos\phi + \psi_n)^2 + \xi_n^2}}\right) - \frac{r_a(\psi_n'' - \eta_n'')\cos^2\alpha}{4\sin^2\alpha} = 0 \tag{21}$$

where prime denotes differentiation with respect to the non-dimensional time τ and the subscripts $n-1$, n, $n+1$ denote displacements in corresponding unit cells of the one-dimensional periodic chain.

5. Asymptotic analysis

5.1. Proximity to global energy minima and perturbation expansion

We assume that the two linear oscillators and the bi-stable mass remain close to their initial equilibrium configuration which are 0, 0 and $\sin\phi$ respectively. This configuration is a global energy minima of the system under consideration. A Taylor series expansion is performed for the nonlinear functions in the equations of motion about those points by taking $\eta_n = 0 + \delta_n$, $\psi_n = 0 + \lambda_n$, $\xi_n = \sin\phi + \zeta_n$. Retaining upto quadratic terms in the expansion, we obtain the equations of motion for the system as:

$$\begin{aligned}\delta_n'' + (\delta_n - \lambda_{n-1}) - \Big(& -\cos^2\phi\,\delta_n + \sin\phi\cos\phi\,\zeta_n \\ & + \frac{1}{2}\Big((3\cos\phi - 3\cos^3\phi)\delta_n^2 \\ & + 2\delta_n\zeta_n(-\sin\phi + 3\sin\phi\cos^2\phi) + (\cos\phi - 3\sin^2\phi\cos\phi)\zeta_n^2 \Big)\Big) \\ & + \chi_a(\lambda_n'' - \delta_n'') = 0\end{aligned} \tag{22}$$

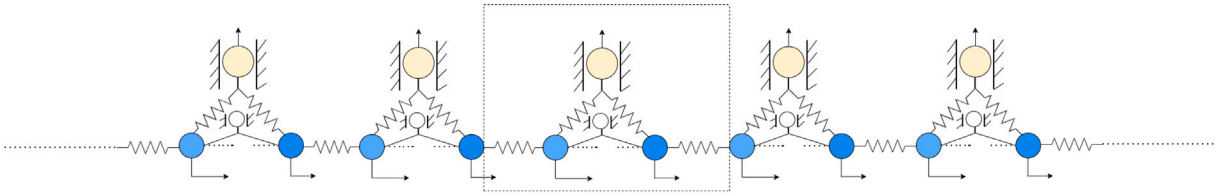

(a) The periodic one-dimensional chain

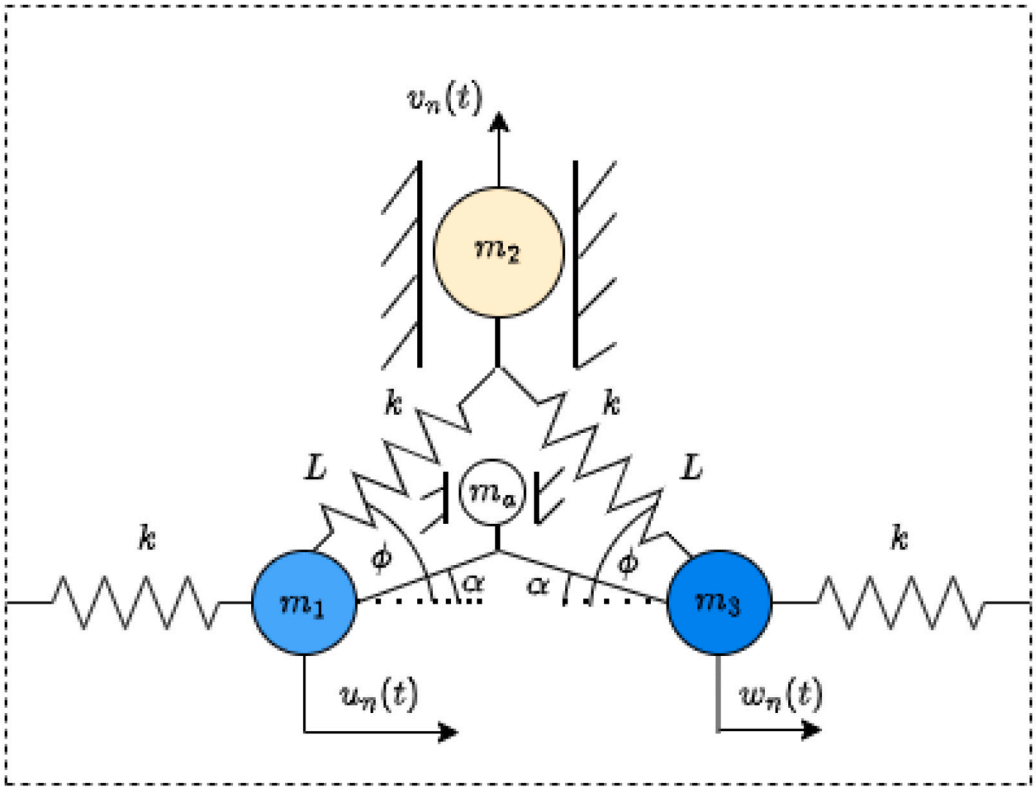

(b) The repeating n-th unit cell

Fig. 5. The periodic chain showing the constitutive repeating unit cell where $u_n(t)$, $w_n(t)$ represent the horizontal degrees of freedom of masses m_1 and m_3 respectively, $v_n(t)$ represents the vertical degree of freedom of the bi-stable mass m_2 in the nth unit cell, k denotes the stiffness co-efficients of all the springs, L denotes the natural length of the springs in the initial undeformed configuration, ϕ denotes the angle of inclination of the inclined linear springs with the horizontal axis in the initial undeformed configuration, α denotes the angle of inclination of the rigid links with the horizontal axis in the initial undeformed configuration.

$$
\begin{aligned}
r_1\zeta_n'' + \Big(& -\sin\phi\cos\phi\delta_n + 2\sin^2\phi\zeta_n + \sin\phi\cos\phi\lambda_n \\
& + \frac{1}{2}\Big(\delta_n^2(\sin\phi - \sin\phi\cos^2\phi) + \zeta_n^2(6\sin\phi - 6\sin^3\phi) \\
& + \lambda_n^2(\sin\phi - 3\sin\phi\cos^2\phi) + 2\delta_n\zeta_n(3\sin^2\phi\cos\phi - \cos\phi) \\
& + 2\delta_n\lambda_n(\cos\phi - 3\sin\phi\cos\phi)\Big)\Big) = 0
\end{aligned} \tag{23}
$$

$$
\begin{aligned}
r_2\lambda_n'' + (\lambda_n - \delta_{n+1}) + \Big(& \sin\phi\cos\phi\zeta_n + \cos^2\phi\lambda_n \\
& + \frac{1}{2}\Big((\cos\phi - 3\sin^2\phi\cos\phi)\zeta_n^2 \\
& + 2\zeta_n\lambda_n(\sin\phi - 3\sin\phi\cos^2\phi) + (3\cos\phi - 3\cos^3\phi)\lambda_n^2\Big)\Big) \\
& - \chi_a(\lambda_n'' - \delta_n'') = 0
\end{aligned} \tag{24}
$$

where, $\chi_a = \frac{r_a\cos^2\alpha}{4\sin^2\alpha}$ is defined as the inertial amplification factor.

According to our previous assumptions that the masses remain very close to their initial equilibrium configurations, an asymptotic expansion is done in Eqs. (22), (23), (24). We introduce a small parameter ϵ dependent upon the initial conditions such that $\delta_n = \epsilon\delta_n^{(0)} + \epsilon^2\delta_n^{(1)}$, $\zeta_n = \epsilon\zeta_n^{(0)} + \epsilon^2\zeta_n^{(1)}$ and $\lambda_n = \epsilon\lambda_n^{(0)} + \epsilon^2\lambda_n^{(1)}$. Inserting the chosen expansion into Eqs. (22), (23), (24), we get the linearized equations at different levels of approximation. We first consider the $O(\epsilon)$ equations to derive the linearized dispersion relations. The $O(\epsilon)$ equations are given as follows:

$$\delta_n^{(0)''} + (\delta_n^{(0)} - \lambda_{n-1}^{(0)}) + \cos^2\phi\delta_n^{(0)} - \sin\phi\cos\phi\zeta_n^{(0)} + \chi_a(\lambda_n^{(0)''} - \delta_n^{(0)''}) = 0 \tag{25}$$

$$r_1\zeta_n^{(0)''} - \sin\phi\cos\phi\delta_n^{(0)} + 2\sin^2\phi\zeta_n^{(0)} + \sin\phi\cos\phi\lambda_n^{(0)} = 0 \tag{26}$$

$$r_2\lambda_n^{(0)''} + (\lambda_n^{(0)} - \delta_{n+1}^{(0)}) + \sin\phi\cos\phi\zeta_n^{(0)} + \cos^2\phi\lambda_n^{(0)} - \chi_a(\lambda_n^{(0)''} - \delta_n^{(0)''}) = 0 \tag{27}$$

These equations are then used in the next Section 5.2 to evaluate the linearized dispersion branches at the first level of approximation.

5.2. Linear dispersion analysis at first level of approximation

To derive the linear dispersion relationship, we apply Bloch's theorem to express the displacements in the successive unit cells in the form shown below.

$$\delta_n^{(0)} = \tilde{\delta}^{(0)} e^{i\mu n} e^{i\omega\tau} \tag{28}$$

$$\zeta_n^{(0)} = \tilde{\zeta}^{(0)} e^{i\mu n} e^{i\omega\tau} \tag{29}$$

$$\lambda_n^{(0)} = \tilde{\lambda}^{(0)} e^{i\mu n} e^{i\omega\tau} \tag{30}$$

where μ is the dimensionless wavenumber and ω is the free wave frequency. Substituting the assumed forms of displacements in the $O(\epsilon)$ equations of motion Eqs. (25), (26) and (27), we obtain the following equations:

$$-\omega^2\tilde{\delta}^{(0)} + (\tilde{\delta}^{(0)} - \tilde{\lambda}^{(0)} e^{-i\mu}) + \cos^2\phi\,\tilde{\delta}^{(0)} - \sin\phi\cos\phi\,\tilde{\zeta}^{(0)} - \chi_a(\tilde{\lambda}^{(0)} - \tilde{\delta}^{(0)}) = 0 \tag{31}$$

$$-\omega^2 r_1\tilde{\zeta}^{(0)} - \sin\phi\cos\phi\,\tilde{\delta}^{(0)} + 2\sin^2\phi\,\tilde{\zeta}^{(0)} + \sin\phi\cos\phi\,\tilde{\lambda}^{(0)} = 0 \tag{32}$$

$$-\omega^2 r_2\tilde{\lambda}^{(0)} + (\tilde{\lambda}^{(0)} - \tilde{\delta}^{(0)} e^{i\mu}) + \sin\phi\cos\phi\,\tilde{\zeta}^{(0)} + \cos^2\phi\,\tilde{\lambda}^{(0)} + \chi_a(\tilde{\lambda}^{(0)} - \tilde{\delta}^{(0)}) = 0 \tag{33}$$

Separating the mass matrix and the wavenumber reduced stiffness matrix in the above three equations, we have

$$[\mathbf{M}] = \begin{bmatrix} 1-\chi_a & 0 & \chi_a \\ 0 & r_1 & 0 \\ \chi_a & 0 & r_2-\chi_a \end{bmatrix} \tag{34}$$

$$[\mathbf{K}(\boldsymbol{\mu})] = \begin{bmatrix} 1+\cos^2\phi & -\sin\phi\cos\phi & -e^{-i\mu} \\ -\sin\phi\cos\phi & 2\sin^2\phi & \sin\phi\cos\phi \\ -e^{i\mu} & \sin\phi\cos\phi & 1+\cos^2\phi \end{bmatrix} \tag{35}$$

Therefore the eigen value problem to derive the dispersion relation is formulated as:

$$([\mathbf{K}(\boldsymbol{\mu})] - \omega^2[\mathbf{M}])\tilde{X}^{(0)} = 0 \tag{36}$$

where $\tilde{X}^{(0)} = \begin{Bmatrix} \tilde{\delta}^{(0)} \\ \tilde{\zeta}^{(0)} \\ \tilde{\lambda}^{(0)} \end{Bmatrix}$. To obtain the dispersion relation we set the determinant of $[\mathbf{K}(\boldsymbol{\mu})] - \omega^2[\mathbf{M}]$ to be equal to zero as is the standard method for obtaining non-trivial solutions.

From the eigenvalue problem described in Eq. (36), we can evaluate the frequencies numerically or analytically for a given specified range of wavenumbers. Since the eigenvalue problem results in a cubic polynomial equation in terms of ω^2, deriving analytical solutions will bring in very complicated and lengthy expressions. So, we solve the eigenvalue problem numerically over the first IBZ. This method of specifying the wavenumber μ and solving for the frequencies ω is known as the inverse method.

5.3. Positive definiteness of the unit cell mass matrix (Sylvester's criterion)

The unit-cell kinetic energy is

$$T = \frac{1}{2}\dot{\mathbf{q}}^T[\mathbf{M}]\dot{\mathbf{q}}, \tag{37}$$

where $\mathbf{q}$ is the generalized displacement vector of a representative repeating unit cell. Hence, physical admissibility requires the real, symmetric mass matrix $[\mathbf{M}]$ to be positive definite so that $T > 0$ for all $\dot{\mathbf{q}} \neq \mathbf{0}$. This also ensures that the generalized eigenvalue problem $[\mathbf{K}(\boldsymbol{\mu})]\tilde{X}^{(0)} = \omega^2[\mathbf{M}]\tilde{X}^{(0)}$ has real eigenvalues ω^2 (for Hermitian $[\mathbf{K}(\boldsymbol{\mu})]$), avoiding spurious non-physical instabilities stemming from an indefinite inertia operator.

For a real symmetric matrix $[\mathbf{M}] \in \mathbb{R}^{n\times n}$, Sylvester's criterion states that $\mathbf{M} \succ \mathbf{0}$ if and only if all leading principal minors are strictly positive:

$$\Delta_k = \det\big([\mathbf{M}]_{1:k,1:k}\big) > 0, \qquad k = 1, 2, \ldots, n. \tag{38}$$

From Eq. (34), the non-dimensional unit cell mass matrix is

$$[\mathbf{M}] = \begin{bmatrix} 1-\chi_a & 0 & \chi_a \\ 0 & r_1 & 0 \\ \chi_a & 0 & r_2-\chi_a \end{bmatrix}, \qquad \chi_a = \frac{r_a\cos^2\alpha}{4\sin^2\alpha}, \tag{39}$$

where χ_a is the inertial-amplification factor. The leading principal minors are

$$\Delta_1 = 1 - \chi_a, \tag{40}$$

$$\Delta_2 = \det\begin{bmatrix} 1-\chi_a & 0 \\ 0 & r_1 \end{bmatrix} = r_1(1-\chi_a), \tag{41}$$

$$\Delta_3 = \det(\mathbf{M}) = r_1 \det\begin{bmatrix} 1-\chi_a & \chi_a \\ \chi_a & r_2-\chi_a \end{bmatrix} = r_1\Big[(1-\chi_a)(r_2-\chi_a) - \chi_a^2\Big] = r_1\Big[r_2 - \chi_a(r_2+1)\Big]. \tag{42}$$

Therefore, $\mathbf{M} \succ \mathbf{0}$ holds if and only if

$$r_1 > 0, \qquad \chi_a < 1, \qquad r_2 > \frac{\chi_a}{1-\chi_a} \quad \Big(\text{equivalently } \chi_a < \frac{r_2}{r_2+1}\Big). \tag{43}$$

The boundary case $\det(\mathbf{M}) = 0$ occurs at

$$r_{2,\text{crit}} = \frac{\chi_a}{1-\chi_a}, \tag{44}$$

beyond which the inertia operator becomes singular/indefinite, and the generalized eigenproblem may yield non-physical (imaginary) frequencies.

For the baseline choice $\sin\alpha = 0.5$ (thus $\cos^2\alpha/(4\sin^2\alpha) = 3/4$) and for $r_a = 0.5$, we obtain

$$\chi_a = \frac{3}{4}r_a = \frac{3}{8}, \qquad r_{2,crit} = \frac{\frac{3}{8}}{1-\frac{3}{8}} = \frac{3/8}{5/8} = \frac{3}{5} = 0.6. \tag{45}$$

Hence, for $r_1 = 1$ and $r_a = 0.5$ (with $\sin\alpha = 0.5$), the unit cell mass matrix is positive definite provided

$$r_2 > 0.6. \tag{46}$$

Similarly, using $\chi_a < \frac{r_2}{r_2+1}$, for the same baseline choice of $\sin\alpha = 0.5$ and taking the value of $r_2 = 1$, we get

$$\frac{3}{4}r_a < \frac{1}{2} \implies r_a < \frac{2}{3} \approx 0.7 \tag{47}$$

keeping upto one significant digit after the decimal place.

5.4. Second-order correction to the dispersion profiles

We now inspect the $O(\epsilon^2)$ equations to investigate the second order corrections in the dispersion profile. The $O(\epsilon^2)$ equations are obtained as follows:

$$\begin{aligned} &\delta_n^{(1)\prime\prime} + (\delta_n^{(1)} - \lambda_{n-1}^{(1)}) + \cos^2\phi\,\delta_n^{(1)} - \sin\phi\cos\phi\,\zeta_n^{(1)} + \chi_a(\lambda_n^{(1)\prime\prime} - \delta_n^{(1)\prime\prime}) \\ &= \frac{1}{2}\Big((3\cos\phi - 3\cos^3\phi)\delta_n^{(0)^2} + 2\delta_n^{(0)}\zeta_n^{(0)}(-\sin\phi + 3\sin\phi\cos^2\phi) \\ &\quad + (\cos\phi - 3\sin^2\phi\cos\phi)\zeta_n^{(0)^2}\Big) \end{aligned} \tag{48}$$

$$\begin{aligned} &r_1\zeta_n^{(1)\prime\prime} - \sin\phi\cos\phi\,\delta_n^{(1)} + 2\sin^2\phi\,\zeta_n^{(1)} + \sin\phi\cos\phi\,\lambda_n^{(1)} \\ &= -\frac{1}{2}\Big(\delta_n^{(0)^2}(\sin\phi - \sin\phi\cos^2\phi) + \zeta_n^{(0)^2}(6\sin\phi - 6\sin^3\phi) \\ &+ \lambda_n^{(0)^2}(\sin\phi - 3\sin\phi\cos^2\phi) \\ &+ 2\delta_n^{(0)}\zeta_n^{(0)}(3\sin^2\phi\cos\phi - \cos\phi) + 2\delta_n^{(0)}\lambda_n^{(0)}(\cos\phi - 3\sin\phi\cos\phi)\Big) \end{aligned} \tag{49}$$

$$\begin{aligned} &r_2\lambda_n^{(1)\prime\prime} + (\lambda_n^{(1)} - \delta_{n+1}^{(1)}) + \sin\phi\cos\phi\,\zeta_n^{(1)} + \cos^2\phi\,\lambda_n^{(1)} - \chi_a(\lambda_n^{(1)\prime\prime} - \delta_n^{(1)\prime\prime}) \\ &= -\frac{1}{2}\Big((\cos\phi - 3\sin^2\phi\cos\phi)\zeta_n^{(0)^2} + 2\zeta_n^{(0)}\lambda_n^{(0)}(\sin\phi - 3\sin\phi\cos^2\phi) \\ &\quad + (3\cos\phi - 3\cos^3\phi)\lambda_n^{(0)^2}\Big) \end{aligned} \tag{50}$$

The left hand sides of the $O(\epsilon^2)$ Eqs. (48), (49) and (50) are same as the left hand side of the $O(\epsilon)$ Eqs. (25), (26), (27) derived before. Hence, we will assume a secular Bloch solution for the equations above and investigate the second order correction to the frequency. We assume a series expansion of the free wave frequency ω in terms of the small parameter ϵ.

$$\omega = \omega_0 + \epsilon\omega_1 + O(\epsilon^2) \tag{51}$$

Now, ω_0 has already been found out in our linear dispersion analysis in Section 5.2 in terms of the wavenumber by solving the eigenvalue problem Eq. (36). We will then evaluate ω_1 in terms of the wavenumber and the amplitude by imposing the secularity condition as done in [11]. The second order correction to the jth frequency $\omega_{1,j}$ is given by

$$\omega_{1,j}(A_0,\mu) = \frac{u_{0,j}^H(\mu)c_1(A_0)}{\omega_{0,j}A_0 u_{0,j}^H(\mu)\mathbf{M}u_{0,j}(\mu)} \tag{52}$$

where $u_{0,j}$ represents the jth normalized complex wave mode or the jth eigenvector to the first order equations, $c_1(A_0)$ represents the coefficient of the first harmonic in the Fourier series expansion of the nonlinear forcing function on the right hand side of the $O(\epsilon^2)$ equations (Eqs. (48)–(50)), $\mathbf{M}$ is the mass matrix, $u_{0,j}^H(\mu)$ is the Hermitian or the complex conjugate transpose of the jth complex wave mode or the normalized eigenvector and A_0 is the free wave amplitude of the $O(\epsilon)$ equations which is considered as a parameter dependent upon the initial conditions. It is worthwhile to note here that this second-order correction to the frequency by imposing the secularity condition will hold true even in the case of a complex μ dependent stiffness matrix [11] and fully populated mass matrix [$\mathbf{M}$] with off-diagonal terms [44].

5.5. Dispersion diagrams from asymptotic analysis

If we vary the three different mass ratios, the dispersion profiles will show varying characteristics. This is a subject of study in the current work, where we will vary the system parameters and study how the dispersion characteristics depend on them.

We first vary the mass ratio r_1 and keep the other parameters same. We vary r_1 from 0.1 to 1 and plot the frequency as a function of wavenumber in Fig. 6 for the following set of values of the other system parameters. $r_a = 0.5, r_2 = 1, \sin\phi = 0.6, \sin\alpha = 0.5$, $\epsilon = 0.1$ The initial conditions at the $O(\epsilon)$ level are taken as

$$\begin{Bmatrix} \delta_n^{(0)} \\ \zeta_n^{(0)} \\ \lambda_n^{(0)} \end{Bmatrix} (\tau = 0) = \begin{Bmatrix} 1 \\ 1 \\ 1 \end{Bmatrix} \tag{53}$$

The initial conditions at $O(\epsilon^2)$ level are all taken to be zero. So the net initial conditions are obtained as

$$\begin{Bmatrix} \delta_n \\ \zeta_n \\ \lambda_n \end{Bmatrix} (\tau = 0) = \epsilon \begin{Bmatrix} 1 \\ 1 \\ 1 \end{Bmatrix} + \epsilon^2 \begin{Bmatrix} 0 \\ 0 \\ 0 \end{Bmatrix} = \begin{Bmatrix} 0.1 \\ 0.1 \\ 0.1 \end{Bmatrix} \tag{54}$$

These set of initial conditions are in agreement with our initial assumption for asymptotic analysis that the masses remain close to their initial equilibrium positions.

Next, we vary the mass ratio r_2 from 0.7 to 1 and plot the dispersion profiles in Fig. 7 with the values of the other parameters kept fixed at $r_a = 0.5, r_1 = 1, \sin\phi = 0.6, \sin\alpha = 0.5$, $\epsilon = 0.1$. The initial conditions are kept the same as before. Below the values of $r_2 = 0.7$, and reducing by one significant digit after the decimal place, i.e. for $r_2 = 0.6, 0.5, \ldots..0.1$ as obtained previously in Section 5.3, Eq. (46), the frequencies become imaginary for the wavenumber varying over the first IBZ, which is not realizable for an undamped physical system like ours. So, we refrain from plotting them.

Next, we vary the inertial amplifier mass ratio r_a from 0.1 to 0.6 and plot the dispersion profiles in Fig. 8. The values of the other system parameters are taken as $r_1 = 1, r_2 = 1, \sin\phi = 0.6, \sin\alpha = 0.5$, $\epsilon = 0.1$. The initial conditions are kept the same as before. Beyond the values of $r_a = 0.6$, and increasing by one significant digit after the decimal place, i.e. for $r_a = 0.7, 0.8.....1$ as obtained in Section 5.3, Eq. (47), the frequencies become imaginary which is not realizable for an undamped physical system. So, we refrain from plotting them.

Physical interpretation of critical thresholds: The critical mass ratio values ($r_2 > 0.6$, $r_a < 0.7$ with baseline angles ϕ and α kept fixed) correspond to dynamic instability boundaries rather than geometric buckling.

For $r_2 \leq 0.6$ (mass m_3 too light): The horizontally oscillating mass m_3 becomes insufficiently inertial to maintain effective coupling with the bistable element m_2. This creates dynamic decoupling where the vertical bistable motion cannot effectively transfer energy to the adjacent unit cell, resulting in evanescent (exponentially decaying) waves rather than propagating waves. Mathematically, this manifests as imaginary frequencies for all $\mu \in [0, \pi]$.

For $r_a > 0.6$ (inertial amplifier mass too large): Excessive inertial amplification creates a negative effective mass effect in the coupled horizontal DOFs. From Eqs. (19) and (21), the inertial amplifier contributes terms $\pm\frac{r_a \cos^2\alpha}{4\sin^2\alpha}$ to the effective mass matrix. When r_a exceeds the critical threshold, these terms dominate and produce negative eigenvalues of the mass matrix, indicating system instability.

These two critical values of r_2 and r_a below which and beyond which traveling waves cannot propagate, with other system parameters kept fixed, are noted down to check as a reference for the strongly nonlinear system.

5.6. Bandgap variation with the mass ratios

We now vary the three different mass ratios one at a time and check how the lower and upper bandgaps vary with them. We also evaluate another quantity which is the difference between the midpoints of the successive frequency curves and plot them alongwith the bandgaps for the three different mass ratios.

First, we vary the mass ratio r_1 from 0.1 to 1 and plot the bandgaps and the midpoint frequency difference (Fig. 9), keeping the other parameters at $r_2 = 1, r_a = 0.5, \sin\phi = 0.6, \sin\alpha = 0.5$. As we can see in Fig. 9, the upper and lower bandgaps more or less show a decreasing pattern with increasing mass ratio r_1. The lower midpoint frequency difference uniformly decreases with increasing r_1. The upper midpoint frequency difference initially decreases upto approximately $r_1 = 0.15$ and the increases with increasing r_1.

Next, we vary the mass ratio r_2 from 0.7 to 0.1 that is the physically realizable region for traveling waves and plot the same quantities i.e. bandgaps and midpoint frequency differences (Fig. 10), keeping the other parameters as $r_1 = 1, r_a = 0.5, \sin\phi = 0.6, \sin\alpha = 0.5$. As we can see from Fig. 10, and as it is evident from the dispersion plots Fig. 7, the lower bandgap and hence the lower midpoint frequency difference remain more or less constant with a very slight decreasing pattern with the mass ratio r_2. The upper bandgap and upper midpoint frequency difference decrease uniformly with r_2.

Finally, we vary the mass ratio r_a from 0.1 to 0.6 that is the physically realizable region for traveling waves and plot the same quantities i.e. bandgaps and midpoint frequency differences (Fig. 11), keeping the other parameters as $r_1 = 1, r_2 = 1, \sin\phi = 0.6, \sin\alpha = 0.5$. As we can see from Fig. 11, and as it is evident from the dispersion plots Fig. 8, the lower bandgap and hence the lower midpoint frequency difference remain more or less constant with a very slight decreasing pattern with the mass ratio r_a. The upper bandgap first decreases upto a value of approximately $r_a = 0.45$ and then increases with r_a. The upper midpoint frequency difference increases uniformly with r_a. Table 2 summarizes the bandgap behavior in the weakly nonlinear regime with critical parameter values specified.

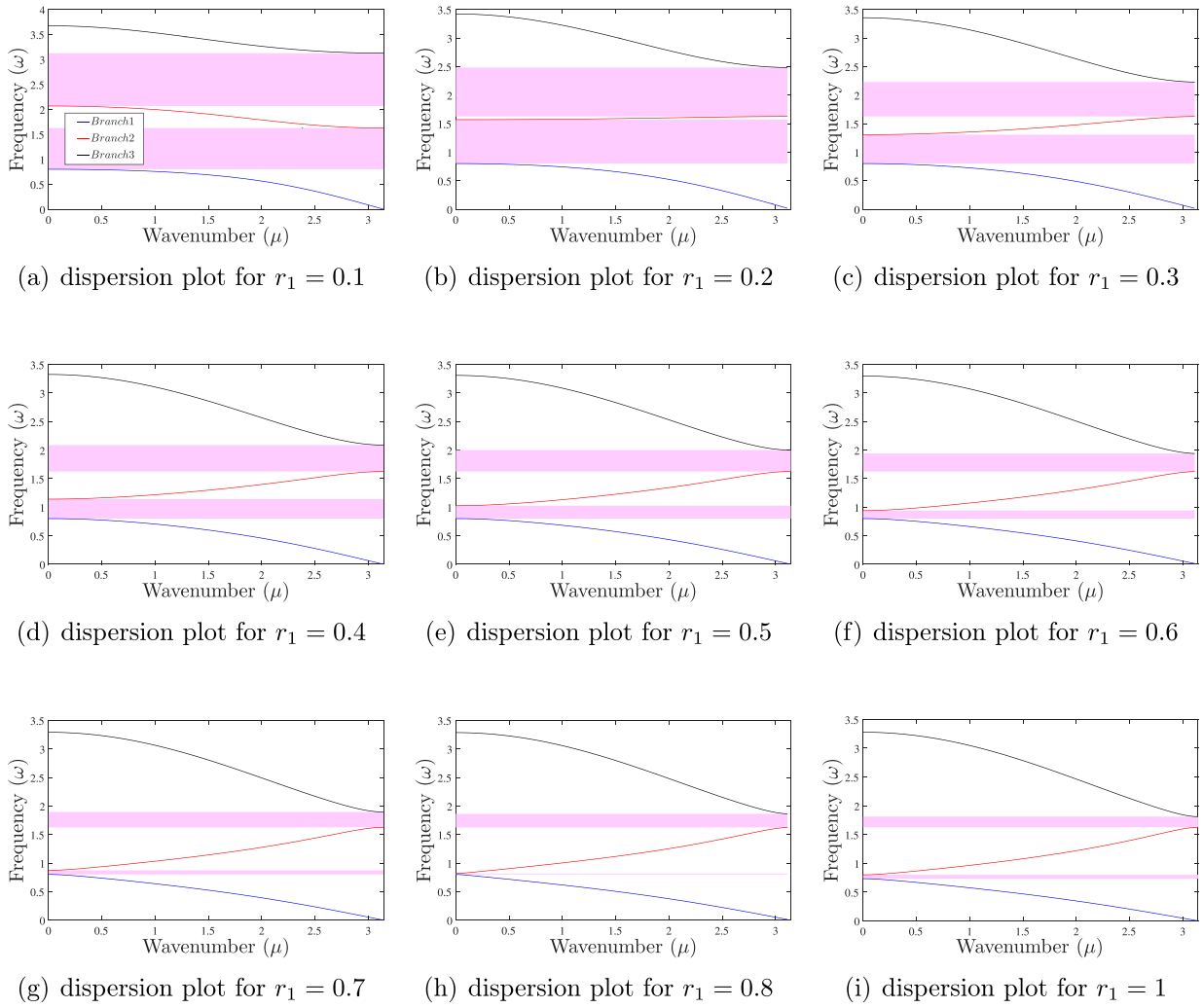

(a) dispersion plot for $r_1 = 0.1$ (b) dispersion plot for $r_1 = 0.2$ (c) dispersion plot for $r_1 = 0.3$

(d) dispersion plot for $r_1 = 0.4$ (e) dispersion plot for $r_1 = 0.5$ (f) dispersion plot for $r_1 = 0.6$

(g) dispersion plot for $r_1 = 0.7$ (h) dispersion plot for $r_1 = 0.8$ (i) dispersion plot for $r_1 = 1$

Fig. 6. Dispersion diagrams from asymptotic analysis showing the three branches of frequency varying with the wavenumber and the relevant bandgaps for mass ratio r_1 varying from 0.1 to 1 and the values of the other parameters kept fixed.

Table 2
Summary of bandgap behavior in weakly nonlinear regime ($\epsilon = 0.1$) for baseline angles $\sin\phi = 0.6$, $\sin\alpha = 0.5$. Trends indicate behavior as parameter increases.

Parameter	Range studied	Lower bandgap trend	Upper bandgap trend	Critical value	Notes
r_1	0.1–1.0	Decreases	Decreases	None	Both branches shift downward
r_2	0.7–1.0	Nearly constant	Decreases	<0.7 (instability)	Strong upper gap sensitivity
r_a	0.1–0.6	Slight decrease	Non-monotonic	>0.6 (instability)	Upper gap: decreases then increases

So, in this section we have indeed manipulated the bandgap by tuning three crucial system parameters that is the three mass ratios. This can come in very useful in analyzing the dynamic behavior of the periodic lattice in its weakly nonlinear regime and also in tuning the wave propagation characteristics of the system such as filtering, vibration attenuation, vibration suppression, etc..

5.7. Dispersion profile by the direct method in the linearized domain

Next, we adopt the direct procedure of plotting the dispersion profiles. From the eigenvalue problem described in Section 5.2, we derive an expression for μ in terms of ω. Expanding the characteristic polynomial in the eigenvalue problem (36), we get the following expression for μ.

$$\cos\mu = \frac{a_1\omega^6 + b_1\omega^4 + c_1\omega^2 + d_1}{a_2\omega^4 + b_2\omega^2 + c_2} \tag{55}$$

where the co-efficients of the different powers of ω are explicitly dependent on the five system parameters r_1, r_2, r_a, ϕ and α. The expressions are not shown here due to very lengthy forms. The frequency ω is varied over a range of values and the real and imaginary parts of the wavenumber are plotted in Fig. 12 for values of the system parameters kept at $r_1 = 1$, $r_2 = 1$, $r_a = 0.5$, $\sin\phi = 0.6$, $\sin\alpha = 0.5$. We can also choose different sets of values of the five system parameters and inspect how the dispersion profile characteristics vary with those values. The real values of the wavenumber μ correspond to propagating waves whereas the imaginary values correspond to attenuating waves.

6. Generalized harmonic balance (HB) method for strongly nonlinear regime

6.1. Generalized harmonic approximation

When the masses in the periodic lattice do not remain very close to their initial equilibrium configuration, the equations of motion

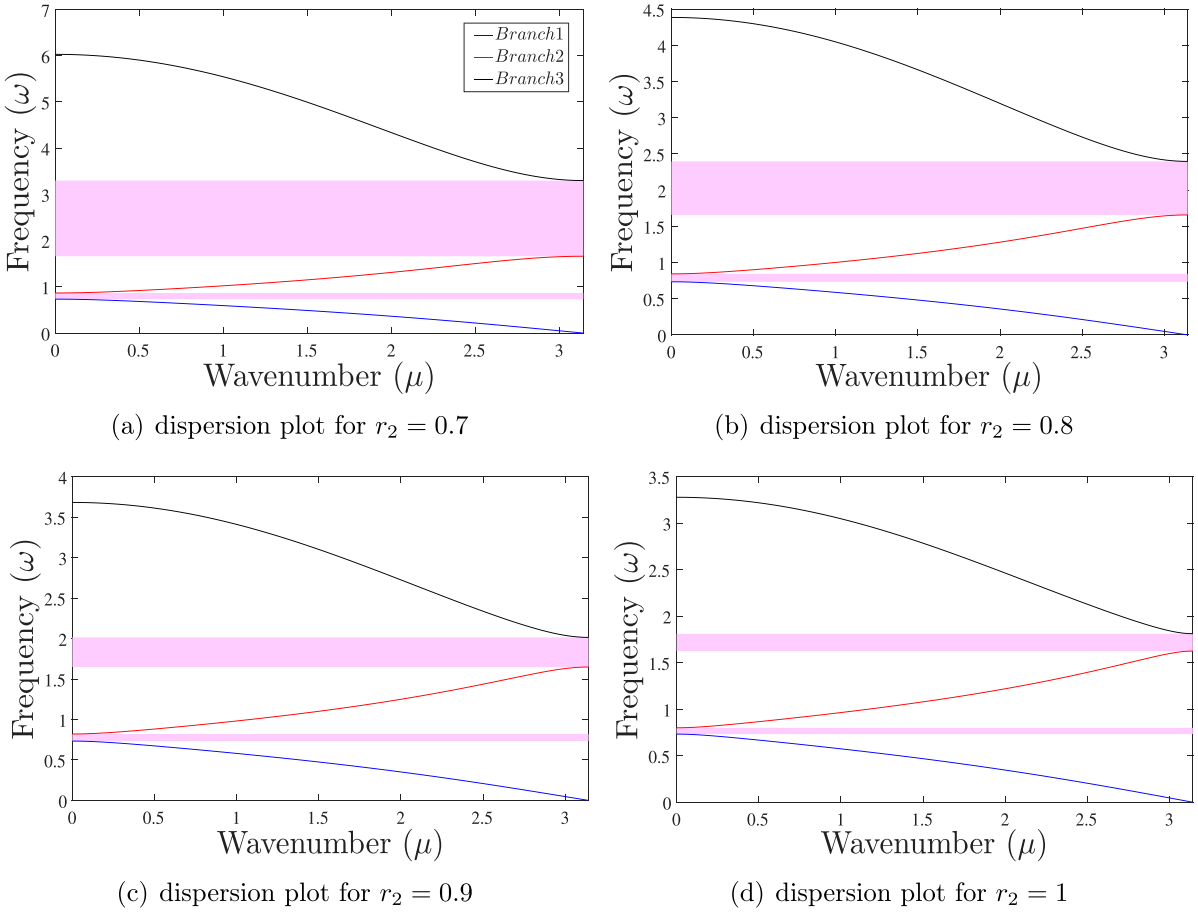

(a) dispersion plot for $r_2 = 0.7$ (b) dispersion plot for $r_2 = 0.8$

(c) dispersion plot for $r_2 = 0.9$ (d) dispersion plot for $r_2 = 1$

Fig. 7. Dispersion diagrams from asymptotic analysis showing the three branches of frequency varying with the wavenumber and the relevant bandgaps for mass ratio r_2 varying from 0.7 to 1 and the values of the other parameters kept fixed.

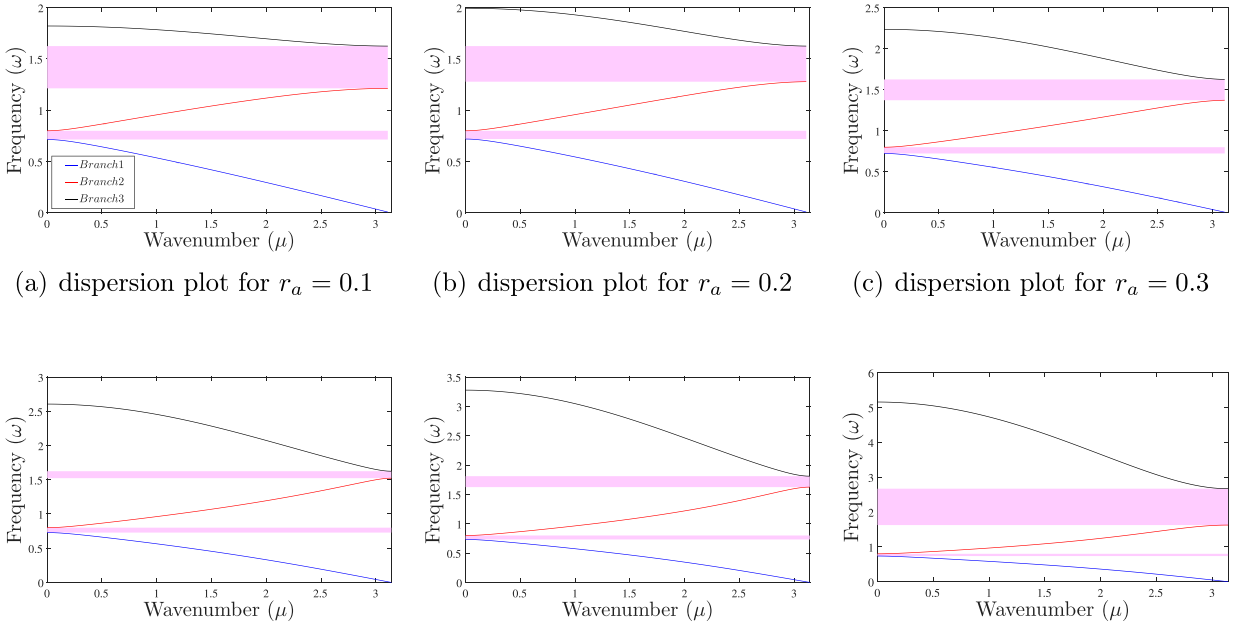

(a) dispersion plot for $r_a = 0.1$ (b) dispersion plot for $r_a = 0.2$ (c) dispersion plot for $r_a = 0.3$

(d) dispersion plot for $r_a = 0.4$ (e) dispersion plot for $r_a = 0.5$ (f) dispersion plot for $r_a = 0.6$

Fig. 8. Dispersion diagrams from asymptotic analysis showing the three branches of frequency varying with the wavenumber and the relevant bandgaps for mass ratio r_a varying from 0.1 to 0.6 and the values of the other parameters kept fixed.

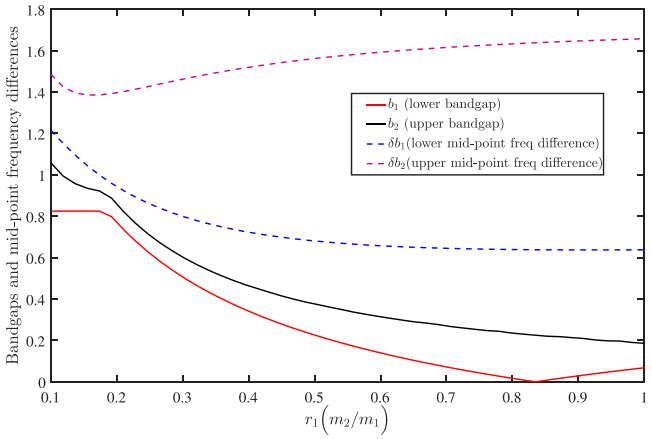

Fig. 9. Bandgap and midpoint frequency difference variation with the mass ratio r_1 keeping all the other parameters fixed.

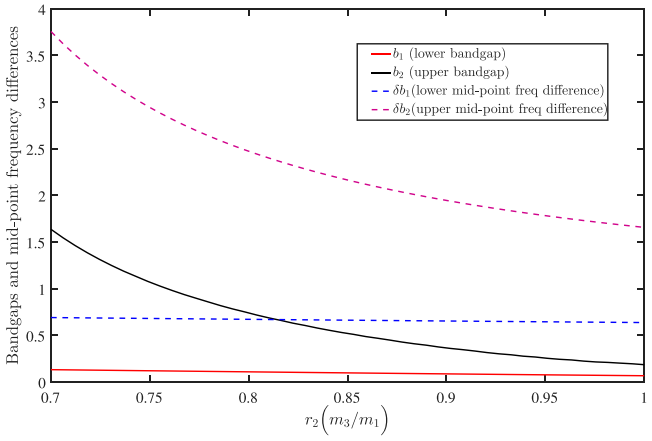

Fig. 10. Bandgap and midpoint frequency difference variation with the mass ratio r_2 keeping all the other parameters fixed.

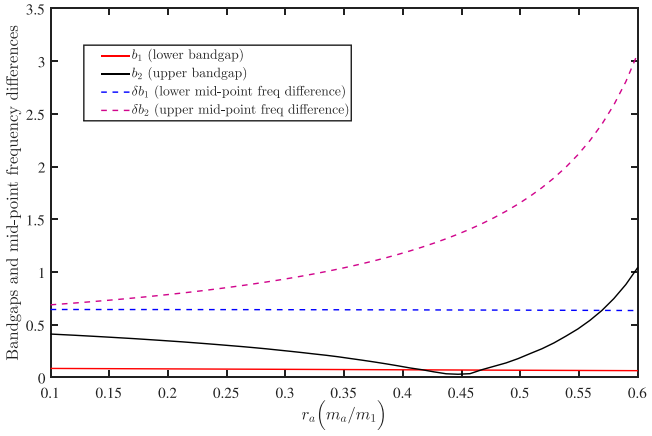

Fig. 11. Bandgap and midpoint frequency difference variation with the mass ratio r_a keeping all the other parameters fixed.

governing the dynamics are strongly nonlinear as is evident from Eqs. (19), (20), (21). So, asymptotic analysis can no longer be used to obtain the time-domain response or the dispersion profiles. Hence, we use a generalized harmonic balance method as done in [11] to obtain the

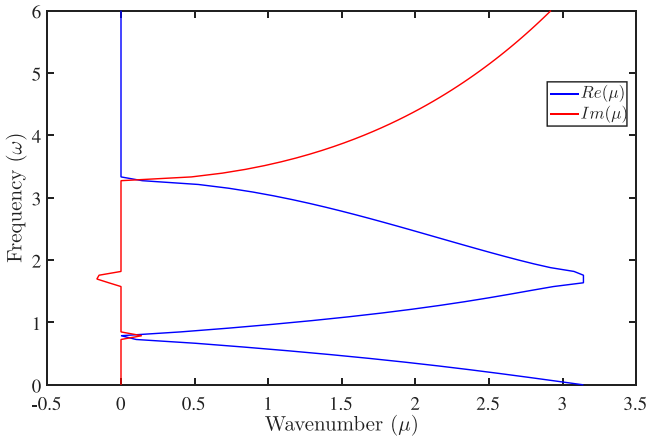

Fig. 12. Dispersion profile showing the real and imaginary parts of the wavenumber for a range of varying frequency.

dispersion profiles. The essence of this method is to assume a Bloch-consistent harmonic expansion for the displacement of the nth unit cell in a general 2-D nonlinear periodic lattice as

$$\mathbf{u}_{\mathbf{n}_1,\mathbf{n}_2} = A\left(\sum_{m=1}^{M} \mathbf{c}_m \cos\left[m(\boldsymbol{\mu}.\mathbf{n} - \omega\tau)\right] + \mathbf{s}_m \sin\left[m(\boldsymbol{\mu}.\mathbf{n} - \omega\tau)\right]\right) \tag{56}$$

where $\boldsymbol{\mu}.\mathbf{n} = \mu_1 n_1 + \mu_2 n_2$ is the inner product of the wavenumber vector with the directional vector of the general 2-D periodic lattice. A is the free wave amplitude which can be considered as an input parameter dependent on the initial conditions, $\mathbf{c}_m$ and $\mathbf{s}_m$ are the unknown harmonic coefficient column vectors to be determined. The key reasoning behind this 'Bloch-consistent' harmonic approximation in the generalized nonlinear regime is the fact that in our chosen periodic model, the nonlinearities are confined within the repeating unit cell and there is no nonlinear coupling between adjacent unit cells as the intercellular horizontal coupling springs have been chosen to have only a linear stiffness coefficient.

Since our system is a 1-D periodic lattice, $n_2 = 0$ and if we choose a unit vector along the axis of our lattice that is the x-axis, then $\boldsymbol{\mu}.\mathbf{n}$ will be just the non-dimensional wavenumber μ. After substitution of Eq. (56) in the governing equations of motion of a general 2-D periodic lattice, and some algebraic manipulations, a set of coupled nonlinear ordinary differential equations is obtained. Then by using Galerkin projection those equations are reduced from differential to algebraic form. Thus, a set of coupled time-independent algebraic equations are obtained with the harmonic co-efficients, the free wave frequency ω, wavenumber μ and the amplitude A as the unknowns. Since our objective is to obtain dispersion relations, we fix μ and A and thus the number of unknowns becomes exactly equal to the number of equations. These equations are then solved by an iterative Newton–Raphson method. We implement this algorithm in Matlab and obtain the dispersion profiles.

6.2. Dispersion profiles obtained using the generalized harmonic balance method

Just like we did for the weakly nonlinear system, here also we will vary the three mass ratios one at a time to get a better understanding of the dispersion characteristics of the system.

First we vary the mass ratio r_1 from 0.1 to 1 and plot the dispersion profiles keeping the other parameters as $r_2 = 1$, $r_a = 0.5$, $\sin\phi = 0.6$, $\sin\alpha = 0.5$. The value of the amplitude parameter A is taken to be 0.1 for a consistent comparison with the results from asymptotic analysis as was done in Section 5.5, Eq. (54). We always choose a number of

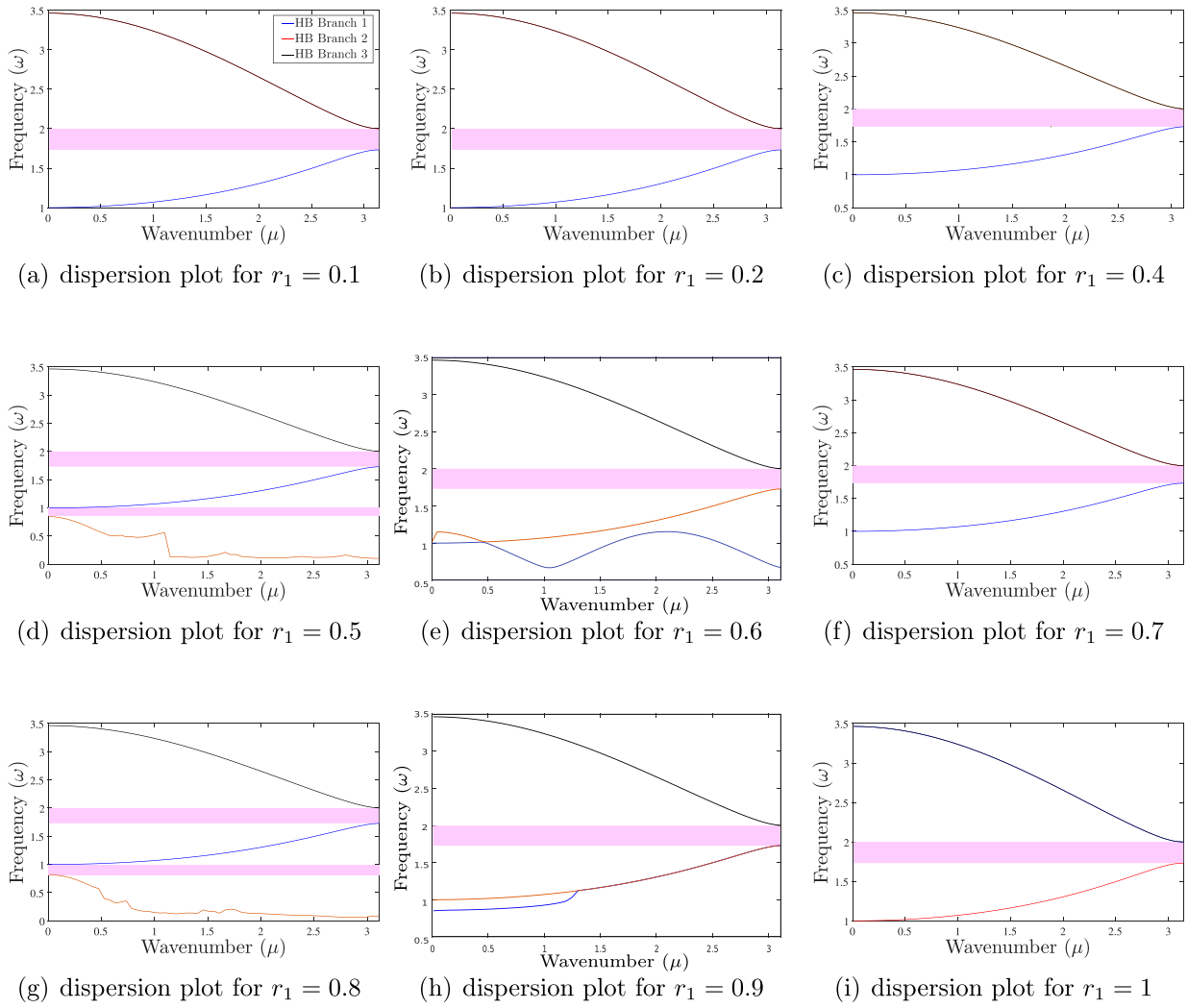

Fig. 13. Dispersion diagrams obtained from the generalized harmonic balance method showing the branches of frequency (ω) varying with the wavenumber (μ) and the relevant bandgaps for mass ratio r_1 varying from 0.1 to 1 and the values of the other parameters kept fixed.

harmonics M such that $M \geq 5$ for smooth dispersion branches in the strongly nonlinear regime.

So, the dispersion profiles are shown with varying mass ratio r_1 in Fig. 13. As we can see for axial wave propagation in our periodic chain, two visible dominant dispersion branches emerge in most of the cases with the third branch partially or fully merging with either one of the other two branches. This can be inferred to the existence of two dominant DOFs in each unit cell with inter-cell coupling with the middle vertical DOF transferring the energy of wave propagation within a particular unit cell between the horizontal DOFs in the strongly nonlinear regime. From $r_1 = 0.1$ to $r_1 = 0.4$, there is not much visible change in bandgap behavior or position of the dispersion branches with branch 2 and branch 3 merging together. The width of the frequently occurring visible bandgap and the average positions of the dispersion branches remain fairly constant with increasing r_1 and the other system parameters kept fixed. Though for some values of r_1 such as $r_1 = 0.5$, 0.8 we notice the emergence of the third dominant branch and a second visible bandgap. Next, our objective will be to examine this behavior of the bandgap and the dispersion branches for the other two mass ratios, r_2 and r_a. This variation of bandgap behavior with non-dimensional system parameters can become very useful in vibration monitoring and vibration isolation.

Next, as discussed, we will vary the mass ratio r_2 from 0.7 to 1 i.e. the stability region observed in the weakly nonlinear regime and plot the dispersion profiles with varying μ in Fig. 14. The other parameters are taken as $r_1 = 1$, $r_a = 0.5$, $\sin\phi = 0.6$, $\sin\alpha = 0.5$. As we can see in Fig. 14, the width of the bandgap decreases steadily from $r_2 = 0.7$ to $r_2 = 1$. We also observe the existence of two visible dominant dispersion branches, with the third branch merging with either of the other two for wave propagation along the axial (horizontal) direction. Also, it can be seen that the two visible dispersion branches shift downwards with increasing r_2. This is in contrast to increasing r_1 before in Fig. 13, where the width of the bandgap and the positions of the dispersion branches remained fairly constant. Below the values of $r_2 = 0.7$ and reducing by one significant digit after the decimal place, i.e. for $r_2 = 0.6, 0.5 \ldots\ldots 0.1$, we observed that one or more the three frequencies go to zero or become imaginary for all values of the wavenumber from 0 to π. Since we are interested in traveling wave solutions in an undamped physical system, we will treat this value of $r_2 = 0.7$ as a lower critical bound (considering one significant digit after the decimal place) with values of r_1 and r_a set to 1 and 0.5 respectively. This outcome is consistent with the behavior in the weakly nonlinear regime where below the same value of $r_2 = 0.7$ (again considering one significant digit after the decimal place) and same other fixed values of the system parameters, we found the frequencies to be imaginary for the same range of varying μ which was again physically not realizable for a traveling wave in the same undamped system.

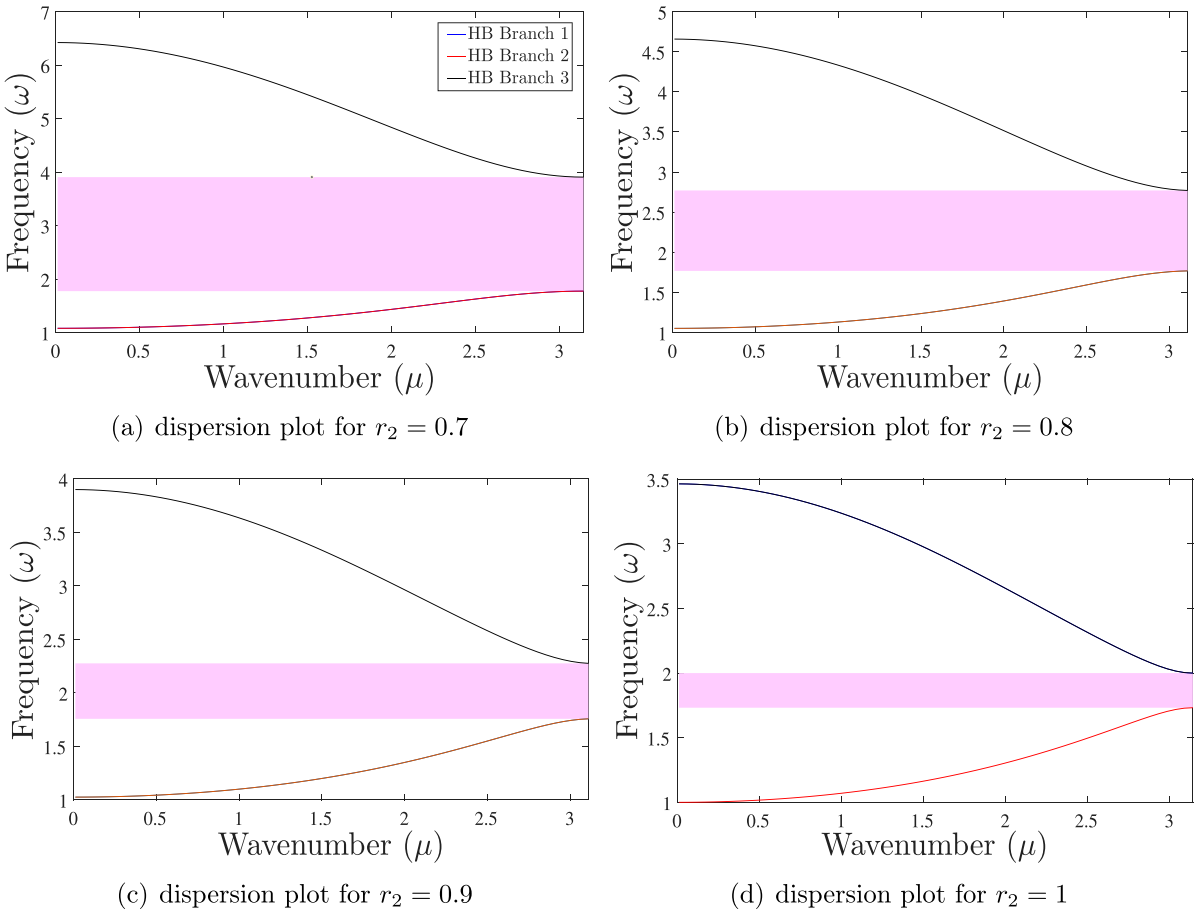

Fig. 14. Dispersion diagrams obtained from the generalized harmonic balance method showing the branches of frequency (ω) varying with the wavenumber (μ) and the relevant bandgaps for mass ratio r_2 varying from 0.7 to 1 and the values of the other parameters kept fixed.

Finally, we vary the mass ratio r_a from 0.1 to 0.6, i.e. the stability region observed in the weakly nonlinear regime and plot the dispersion profiles for the same range of μ in Fig. 15. The other parameters are taken as $r_1 = 1$, $r_2 = 1$, $\sin\phi = 0.6$, $\sin\alpha = 0.5$. Just like the cases of varying r_1 and r_2, here also we observe mostly the existence of two dominant visible dispersion branches in Fig. 15 participating in wave propagation along the axial direction. There is a third branch because of our chosen 3 DOF unit cell, but in most of the cases, it merges with either one of the other two branches producing two visible branches as the net output. The width of the prominent visible bandgap decreases steadily from $r_a = 0.1$ up to $r_a = 0.4$ and then remains fairly constant up to $r_a = 0.5$. At $r_a = 0.6$, the upper bandgap increases more in width and we see the emergence of a third trivial branch near zero which remains fairly constant over the wavenumber μ. One more visible feature to note is that both the visible, non-trivial, dominant branches of the frequency shift upward with increasing r_a, with the shift being more prominent for the higher branch. This is in contrast to increasing r_2 where both the branches shifted downwards in Fig. 14. Beyond the values of $r_a = 0.6$ and increasing by one significant digit after the decimal place,i.e. for $r_a = 0.7, 0.8 \ldots 1$, we observe as in the previous case that one or more of the frequencies become imaginary for all μ which is not realizable for an undamped physical system. The emergence of the third trivial branch near zero at $r_a = 0.6$ might be due to close proximity to the critical zone for the system parameters. As was observed in the previous case of varying r_2, beyond this same value of $r_a = 0.6$ (considering one significant digit after the decimal place), for the weakly nonlinear regime, we had imaginary values of the frequency for the same range of μ and same values of the other system parameters.

Understanding branch merging in the strongly nonlinear regime: Despite three DOFs per unit cell (η, ξ, ψ), predominantly two dominant dispersion branches emerge for axial wave propagation (Figs. 13–15). This phenomenon reflects modal energy redistribution among coupled DOFs. For axial propagation, the horizontal DOFs (η, ψ) dominate inter-cell wave transmission through the horizontal springs (k-stiffness connections between unit cells). The vertical bi-stable DOF (ξ) participates primarily in intra-cell energy transfer, coupling the two horizontal masses within each unit cell but not directly transmitting waves between cells.

Figs. 16(a)–16(c) report the projection-based modal participation fractions obtained by projecting the HB solution for all the three dispersion branches at each wavenumber μ onto the corresponding linear Bloch eigenvectors and normalizing the squared projection amplitudes such that $\sum_{i=1}^{3} p_i(\mu) = 1$. A representative combination of mass ratios $r_1 = 0.2, r_2 = 1, r_a = 0.5$, i.e. the same as chosen for Fig. 13(b) is considered to perform this modal participation analysis. While Branch 1 exhibits a progressive transfer of participation from linear mode 1 to linear mode 2 as μ increases (Fig. 16(a)), Branches 2 and 3 display identical participation trends (Figs. 16(b), 16(c)). Both are dominated by linear mode 3 over most of the Brillouin zone, with a growing contribution from mode 1 toward the zone boundary. This near-coincidence of the modal participation signatures indicates that, in the parameter set considered, the HB solutions on Branches 2 and 3 occupy essentially the same linear modal subspace, i.e., they correspond to the same

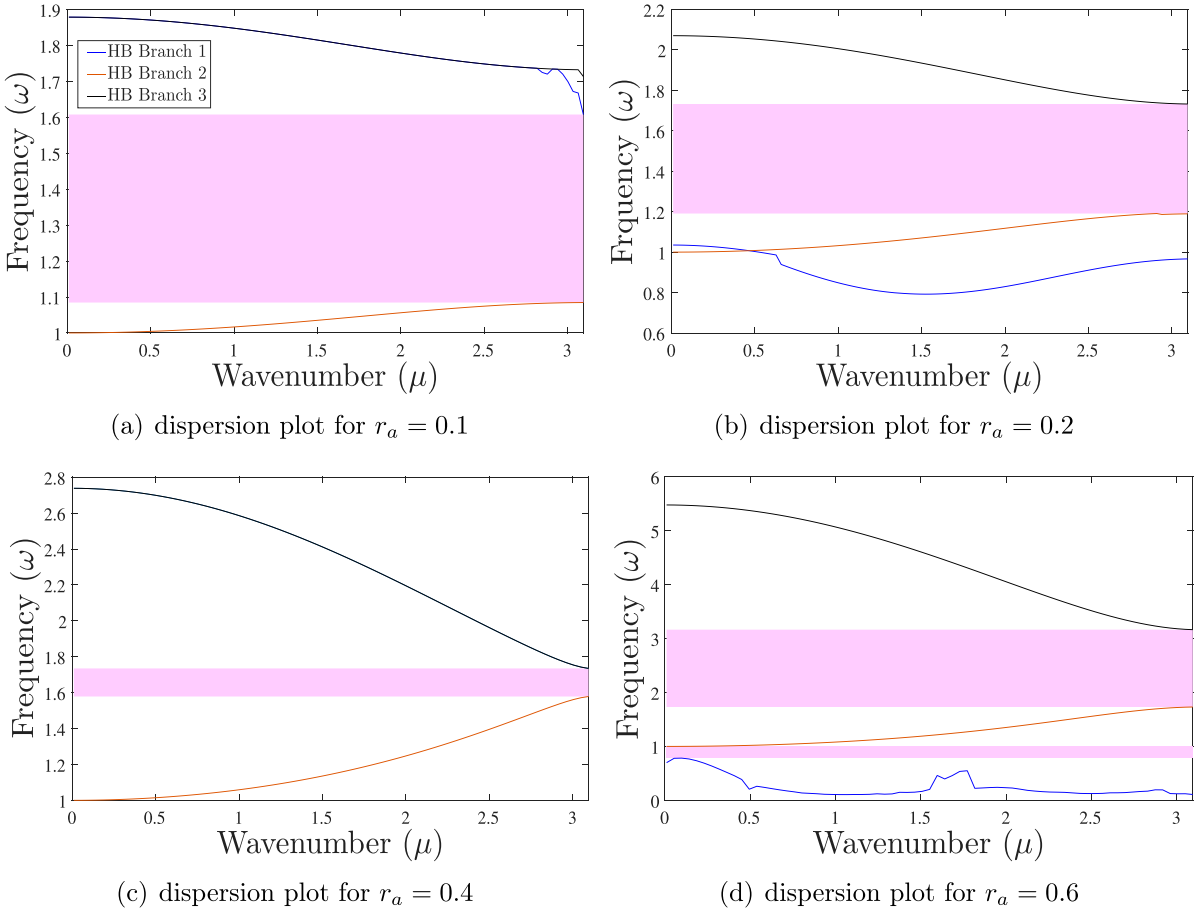

(a) dispersion plot for $r_a = 0.1$ (b) dispersion plot for $r_a = 0.2$

(c) dispersion plot for $r_a = 0.4$ (d) dispersion plot for $r_a = 0.6$

Fig. 15. Dispersion diagrams obtained from the generalized harmonic balance method showing the branches of frequency (ω) varying with the wavenumber (μ) and the relevant bandgaps for mass ratio r_a varying from 0.1 to 0.6 and the values of the other parameters kept fixed.

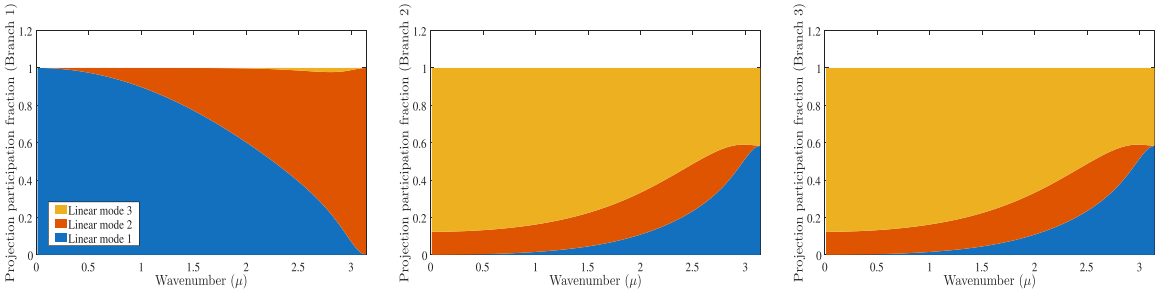

(a) Modal participation fraction for HB Branch 1 (b) Modal participation fraction for HB Branch 2 (c) Modal participation fraction for HB Branch 3

Fig. 16. Modal participation fractions along the HB dispersion branches for $r_1 = 0.2, r_2 = 1, r_a = 0.5$, which is the same combination of mass ratios as chosen in Fig. 13(b), stacked areas show the normalized projection of the HB solution onto the three linear eigenmodes versus wavenumber (μ), the identical modal content of HB Branches 2 and 3 at all μ is consistent with their observed merging in Fig. 13(b).

hybridized periodic motion. Consequently, their dispersion curves HB Branch 2 and HB Branch 3 coalesce, which is observed as the merging of Branches 2 and 3 in the HB dispersion plot in Fig. 13(b).

The weak 'jagged' variations seen on some HB branches in Figs. 13, 15 are most pronounced near branch-merging/band-edge regions, where the vertical bi-stable DOF ξ behaves as a nonlinear internal resonator and intermittently exchanges energy with the horizontal DOFs (η, ψ) and higher harmonics. In these intervals, small changes in wavenumber μ can produce noticeable changes in harmonic content and even nearby coexisting periodic states, so the reported fundamental frequency $\omega(\mu)$ may exhibit mild ripples rather than a perfectly smooth trend.

Table 3 summarizes the bandgap behavior in the strongly nonlinear regime. Tables 2 and 3 synthesize parametric trends observed across Figs. 6–8 and Figs. 13–15 respectively. Key observations: (i) Critical threshold values are consistent across weakly and strongly nonlinear regimes, validating them as fundamental stability boundaries. (ii) The lower bandgap shows relatively consistent behavior across mass ratio variations in both regimes. (iii) The upper bandgap exhibits strong sensitivity to r_2 and r_a, offering design handles for bandgap tuning. (iv) In

Table 3
Summary of bandgap behavior in strongly nonlinear regime for baseline angles $\sin\phi = 0.6$, $\sin\alpha = 0.5$. Trends indicate behavior as parameter increases.

Parameter	Range studied	Lower bandgap trend	Upper bandgap trend	Dominant branches	Critical value	Notes
r_1	0.1–1.0	Approximately constant	Approximately constant	2 (merged)	None	Branch merging patterns vary
r_2	0.7–1.0	Nearly constant	Decreases strongly	2 (merged)	<0.7 (instability)	Branches shift downward
r_a	0.1–0.6	Slight decrease	Non-monotonic	2 (merged)	>0.6 (instability)	Third trivial branch emerges at $r_a = 0.6$

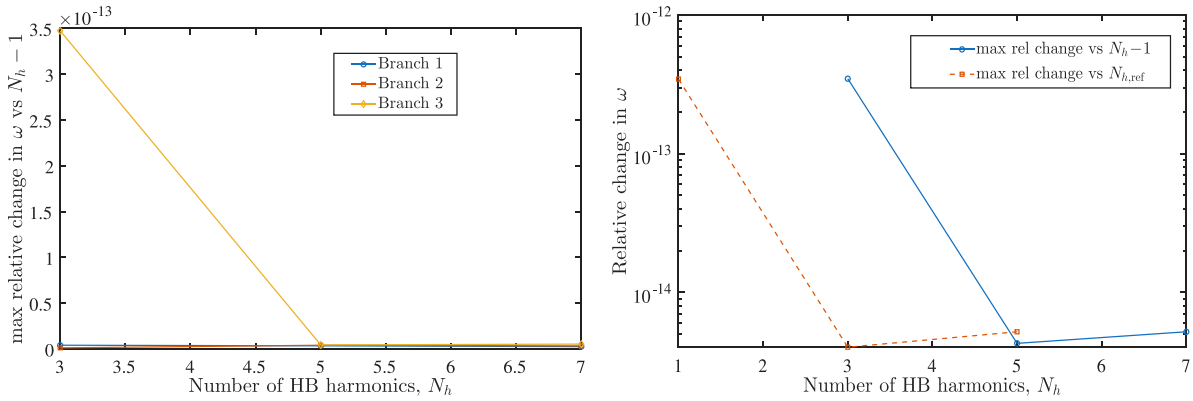

(a) Branch-wise maximum relative change in the HB frequency ω when increasing the harmonic truncation N_h (relative to the preceding N_h in the list).

(b) Global convergence metrics for the HB dispersion: maximum relative change in ω versus N_h, computed (i) against the preceding N_h and (ii) against the reference $N_{h,\mathrm{ref}} = 7$.

Fig. 17. Branch-wise and global convergence metrics for HB dispersion with increasing HB truncation N_h using the same parameter set as in Fig. 13(a).

Table 4
(HB convergence study) Maximum and RMS relative changes in the HB-predicted dispersion frequency $\omega(\mu)$ when increasing the number of retained harmonics $N_h \in \{1,3,5,7\}$ with $N_{h,\mathrm{ref}} = 7$ as reference, evaluated over $\mu \in [0.01, 0.5\pi]$ sampled at five points, 'previous' denotes the preceding N_h in the list, mass ratio combination is taken the same as for Fig. 13(a).

N_h	$\max_\mu \lvert\Delta\omega/\omega\rvert$ (vs. previous)	$\mathrm{RMS}_\mu \lvert\Delta\omega/\omega\rvert$ (vs. previous)	$\max_\mu \lvert\Delta\omega/\omega\rvert$ (vs. $N_{h,\mathrm{ref}} = 7$)	$\mathrm{RMS}_\mu \lvert\Delta\omega/\omega\rvert$ (vs. $N_{h,\mathrm{ref}} = 7$)
1	–	–	3.45×10^{-13}	8.91×10^{-14}
3	3.47×10^{-13}	8.97×10^{-14}	4.01×10^{-15}	1.61×10^{-15}
5	4.28×10^{-15}	2.30×10^{-15}	5.18×10^{-15}	2.26×10^{-15}
7	5.18×10^{-15}	2.26×10^{-15}	0	0

the strongly nonlinear regime, branch merging reduces three nominal branches to two dominant branches, reflecting modal redistribution.

This modal behavior is characteristic of systems with strong geometric coupling between orthogonal DOFs and represents genuine physical modal interaction, not numerical artifact. Direct time-domain simulations (Section 7) confirm that predominantly two frequencies dominate the steady-state response at most wavenumbers, validating the branch merging observed in harmonic balance analysis.

Convergence with respect to the HB harmonic truncation: We repeated the HB dispersion computation for $N_h = \{1,3,5,7\}$ (with time grid $N_t = 512\,N_h$) using the mass ratio combination of Fig. 13(a), i.e., $r_1 = 0.1, r_2 = 1, r_a = 0.5$, and $\sin\phi = 0.6$, $\sin\alpha = 0.5$, and $A = 0.1$, but on a reduced wavenumber grid $\mu \in [0.01, 0.5\pi]$ sampled at five points. Taking $N_{h,\mathrm{ref}} = 7$ as the reference, we evaluated the maximum and RMS relative changes in the predicted dispersion frequency, both (i) between successive truncations N_h and the preceding case in the list and (ii) relative to $N_{h,\mathrm{ref}}$. The branch-wise and global convergence trends (Figs. 17(a) and 17(b)) show rapid saturation. The maximum relative deviation drops to $O(10^{-15})$ for $N_h = 3$ to 5, and the change between $N_h = 5$ and 7 remains below 6×10^{-15} as reported in Table 4. Accordingly, we have used $N_h \geq 5$ for the HB results reported in this work.

6.3. Comparison of HB results with results from asymptotic analysis

Now, we compare the dispersion results obtained from HB method with the dispersion results obtained from asymptotic/perturbation analysis in Section 5.5. We choose four sets of values of the system parameters r_1, r_2, r_a, keeping the initial angles of inclination fixed at $\sin\phi = 0.6$ and $\sin\alpha = 0.5$ and plot the dispersion profiles in Fig. 18.

As we can see from the comparison between the two methods in Fig. 18, the HB branches lie a bit higher than the asymptotic branches which is quite expected for hardening springs as in our case. The more we consider the number of terms in the Taylor series expansion around the global energy minima for asymptotic analysis, the more the dispersion branches obtained using the perturbation method will approach the branches obtained using HB method. One more observation is that for the HB method used for the strongly nonlinear regime in most of the cases keeping r_1 constant at $r_1 = 1$ (Figs. 18(a), 18(b), 18(c)), branch 1 (blue solid) merges with either branch 3 (yellow solid) or branch 2 (red solid), while for the asymptotic analysis, branch 1 (blue dashed) remains separate which again proves the partial failure of perturbation method for the strongly nonlinear regime. But, still it can be said that the perturbation method can provide a basis linear framework for predicting dispersion branches even for a fairly intricate, geometrically nonlinear system such as our model and reduce the computational cost effectively for atleast a considerable number of branches.

7. Time-domain simulation of the finite chain and comparison with HB results

7.1. Inverse Method (IM)

We now use direct numerical time-domain simulation of a finite chain composed of our chosen repeating unit cell to verify our semi-analytical (HB) results. We use the approach in [45] to obtain dispersion relations of a large enough finite chain consisting of 300 unit cells and free at both ends. We use an inverse method to obtain the dispersion relations to compare with our semi-analytical results

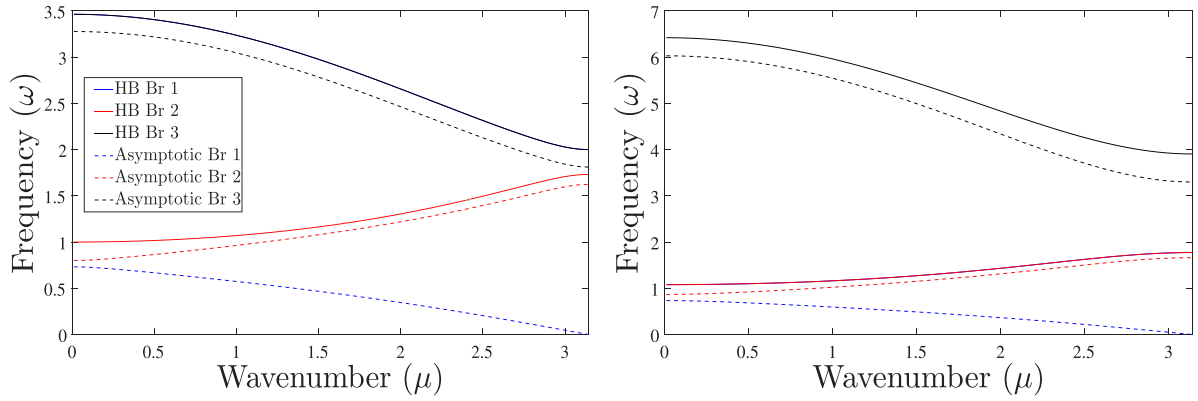

(a) Comparison of dispersion profiles for $r_1 = 1$, $r_2 = 1$, $r_a = 0.5$

(b) Comparison of dispersion profiles for $r_1 = 1$, $r_2 = 0.7$, $r_a = 0.5$

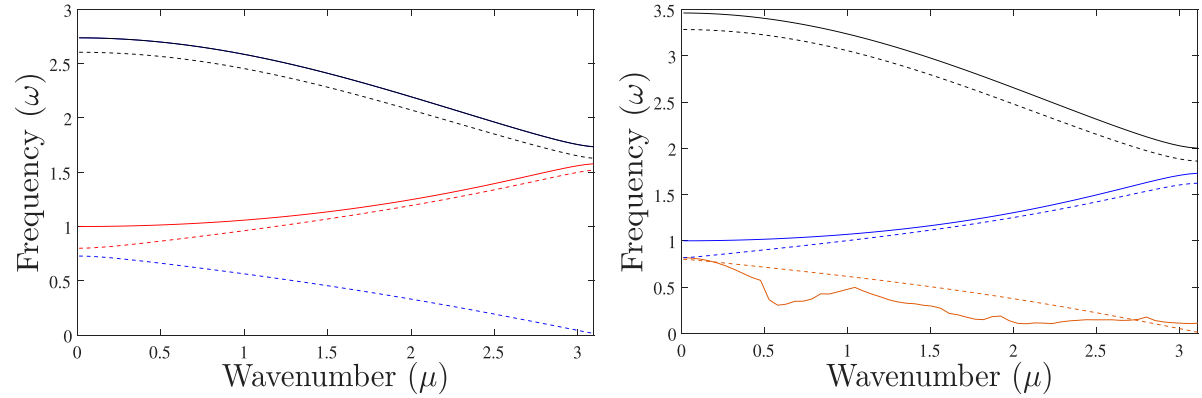

(c) Comparison of dispersion profiles for $r_1 = 1$, $r_2 = 1$, $r_a = 0.4$

(d) Comparison of dispersion profiles for $r_1 = 0.8$, $r_2 = 1$, $r_a = 0.5$

Fig. 18. Comparison of dispersion profiles obtained using HB method and asymptotic analysis for four different sets of values of the mass ratios keeping the initial angles of inclination of the springs and rigid links at $\sin\phi = 0.6$ and $\sin\alpha = 0.5$ respectively. (For interpretation of the references to color in this figure legend, the reader is referred to the web version of this article.)

obtained using the generalized Harmonic Balance Method for the infinite periodic chain in the strongly nonlinear regime. This indeed means that we simulate our exact nonlinear equations of motion in the time-domain. We impose the wavenumber for our structure as an initial condition and release the system in time and then obtain the frequency corresponding to that imposed wavenumber from the time-domain results of a chosen measurement region far away from both boundaries or the reference unit cell located in the middle of the structure. We consider our exact nonlinear and non-dimensionalized equations of motion Eqs. (19)–(21) and choose our initial conditions as follows.

$$
\begin{aligned}
\eta_j(0) &= \sum_{m=1}^{N_h}\left[A_{\eta m}\cos\big(m\mu(j-j_0)\big) + B_{\eta m}\sin\big(m\mu(j-j_0)\big)\right]\\
\dot{\eta}_j(0) &= 0\\
\xi_j(0) &= \sum_{m=1}^{N_h}\left[A_{\xi m}\cos\big(m\mu(j-j_0)\big) + B_{\xi m}\sin\big(m\mu(j-j_0)\big)\right]\\
\dot{\xi}_j(0) &= 0\\
\psi_j(0) &= \sum_{m=1}^{N_h}\left[A_{\psi m}\cos\big(m\mu(j-j_0)\big) + B_{\psi m}\sin\big(m\mu(j-j_0)\big)\right]\\
\dot{\psi}_j(0) &= 0\\
j &\in \{1,\ldots,300\}
\end{aligned}
\tag{57}
$$

So, the initial velocities of the masses are considered to be 0 and we impose an initial spatial wave displacement dependent on the wavenumber μ. The reference unit cell j_0 is chosen in the middle of the chain to minimize boundary effects. N_h is the number of harmonic terms considered for theoretical (HB) results. The amplitudes of the different harmonics $A_{\eta m}$, $B_{\eta m}$, $A_{\xi m}$, $B_{\xi m}$, $A_{\psi m}$, $B_{\psi m}$ are chosen based on the corresponding amplitudes obtained from the Harmonic Balance (HB) method after convergence of the Newton–Raphson algorithm. We choose to iterate every new input amplitude based on a linear scaling factor determined by the previous output amplitude and use this linear scaling factor as an individual gain to update each of the three initial/input amplitudes individually in every iteration until they reach the targets set by the HB method within a certain tolerance (5×10^{-4}). We also use a damping profile which is maximum at the boundaries of our finite chain and decreases almost exponentially to zero in the middle of the chain to minimize the boundary effects as done in [45]. We apply the damping on the horizontally moving masses represented by η and ψ in every unit cell since they are the masses with inter-cell connections.

After convergence, we neglect the initial transients that might be arising from numerical issues, by allowing a settling time of $25T_0$, where $T_0 = \frac{2\pi}{\omega}$ and ω is the frequency already obtained from the HB method. Then, we extract the frequency from the time-domain results by using two methods. We consider the time-domain response of the reference

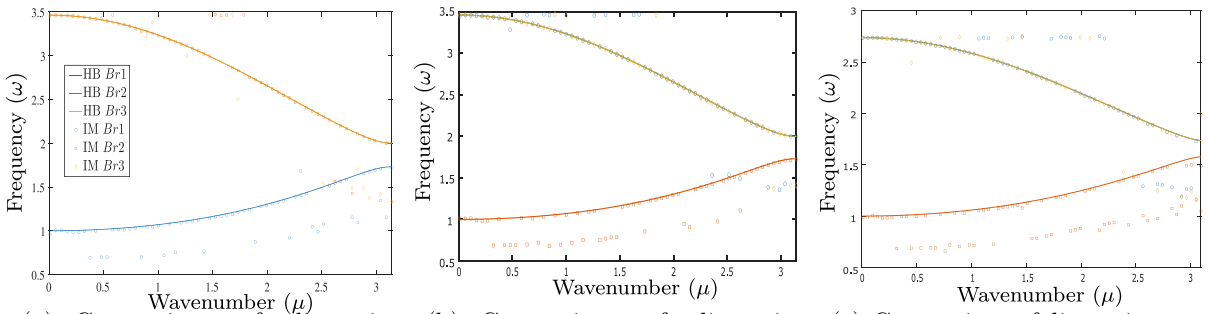

(a) Comparison of dispersion profiles for $r_1 = 0.1$, $r_2 = 1$, $r_a = 0.5$

(b) Comparison of dispersion profiles for $r_1 = 1$, $r_2 = 1$, $r_a = 0.5$

(c) Comparison of dispersion profiles for $r_1 = 1$, $r_2 = 1$, $r_a = 0.4$

Fig. 19. Comparison of harmonic balance (HB) results with direct time-domain (IM) simulations (wavenumber μ vs. frequency ω) for three different sets of values of mass ratios keeping the initial angles of inclination of the springs and rigid links at $\sin\phi = 0.6$ and $\sin\alpha = 0.5$ respectively.

unit cell located at j_0 and measure the global frequency by calculating the average time-period. Next, we choose a measurement region consisting of 30 unit cells in the center of the chain and use a complex spatial demodulation factor to eliminate noise from displacements in the time-domain. Then, we estimate the branch frequency directly from the time-domain response using a phase-slope method anchored to the Harmonic Balance target. The time-domain signal is first resampled onto a uniform grid and, when sufficient cycles are present, passed through a zero-phase third-order Butterworth band-pass centered at the target angular frequency with a relative half-bandwidth. For real inputs we form the analytic signal with the Hilbert transform (complex inputs skip this step), unwrap its phase, and fit a straight line to the central 10–90% of the record, the slope yields the frequency estimate, while the median envelope over the same window gives a robust output amplitude. The procedure is tolerant to uneven sampling and slow drifts, and includes guards for short/noisy records; if the phase fit is ill-conditioned, it falls back to a simple zero-crossing estimate. After we evaluate the frequency from these two procedures, we report the one closest to that obtained using the Harmonic Balance method for that specific wavenumber.

We use a sufficiently large number of harmonics ($N_h \geq 5$) for the HB method to obtain smoother results. So, the net target amplitude set for a DOF to achieve in direct time-domain simulation is obtained through a rough approximation by taking the root mean square (RMS) of the amplitudes ($A_{\eta m}$, $B_{\eta m}$, $A_{\xi m}$, $B_{\xi m}$, $A_{\psi m}$, $B_{\psi m}$) of the different harmonics.

7.2. Dispersion plots showing comparison between harmonic balance and IM results, an error quantification and computational speedup

We now show three dispersion plots (Fig. 19) showing the comparison between harmonic balance (HB) results and the results obtained by direct time-domain simulation using the inverse method discussed in the previous section. We choose three representative sets of values of system parameters as in the mass ratios r_1, r_2, r_a and keep our initial angles in the unstressed equilibrium configuration fixed at $\sin\phi = 0.6$ and $\sin\alpha = 0.5$. We use the explicit ode45 solver in Matlab to run our time-domain simulations. We also keep the value of $r_2 = \frac{m_3}{m_1}$ at 1 to maintain the spatial symmetry of the unit cell to avoid the issues of non-similarity and energy-dependence of the modal curves as much as possible.

Figs. 19(a)–19(c) might look the same quantitatively, but there is a qualitative difference. In Fig. 19(a), branch 2 merges with branch 3 for both semi-analytical HB model and numerical IM model, and effectively we see two dominant branches which is according to our expectations for the strongly nonlinear regime as discussed in Section 6. In Figs. 19(b) and 19(c), we notice the same branch merging and effective existence of two dominant branches but in this case, branch 1 merges with branch 3 for both analytical and time-domain simulation results.

Table 5
Relative error metrics between the Harmonic Balance (HB) dispersion predictions and the Inverse Method (IM) time-domain validation. The pointwise relative error is defined as $e(\mu) = \left|\frac{\omega_{\mathrm{IM}}(\mu) - \omega_{\mathrm{HB}}(\mu)}{\omega_{\mathrm{HB}}(\mu)}\right|$. Reported values are computed over all sampled wavenumbers for each dispersion branch for a combination of mass ratios taken the same as for Fig. 19(a).

Branch	Mean rel. error $\bar{e}$	RMS rel. error e_{rms}	Max rel. error $e_{\max}$
1	0.0863	0.158	0.333
2	0.0408	0.105	0.333
3	0.0619	0.128	0.333

We show an explicit error quantification between dispersion results obtained from the HB method and direct time-domain IM method in Table 5. We choose the values of the mass ratios as $r_1 = 0.1, r_2 = 1, r_a = 0.5$ which is the same combination of mass ratios as chosen in Fig. 19(a), keeping the initial angles of inclination of the springs and rigid links at $\sin\phi = 0.6$ and $\sin\alpha = 0.5$ respectively. For each of the three dispersion branches, we evaluate the relative error $\left|\frac{\omega_{\mathrm{IM}}(\mu) - \omega_{\mathrm{HB}}(\mu)}{\omega_{\mathrm{HB}}(\mu)}\right|$ and report the mean, maximum and rms relative errors in Table 5.

The raw relative error is also plotted against the wavenumber μ in Fig. 20. The HB method took a time of 865.91 s or approximately 14.4 min to implement in a Matlab platform on a single-processor machine. The direct time-domain integration or IM method for our chosen finite chain comprising of 300 unit cells took 3997.40 s or approximately 1.1 h to implement in a Matlab platform on the same machine. So, it can bee seen that the HB method provides a computational speedup of at least 4.5 times than direct time-domain simulations while still predicting the dispersion behavior in the generalized strongly nonlinear regime with a significant level of accuracy.

7.3. Discussion of the comparison between time-domain simulation and HB results, possible chaos and nonlinear modal interactions

As we can see from the results in our previous Section 7.2, the frequency values obtained by time-domain simulation of our exact nonlinear, long enough, finite periodic chain match quite well with the patterns obtained from the HB method for most of the values of the wavenumber (μ). But, we also notice some outliers for some values of the wavenumber. To further investigate this disparity at some places, we shift our focus onto checking whether our system in the strongly nonlinear regime shows transient chaos as discussed when proposing the unit cell model in Section 2. We check the time-domain behavior of our periodic chain for some specific values of wavenumber μ to check if the long-term behavior is aperiodic since that is one of the

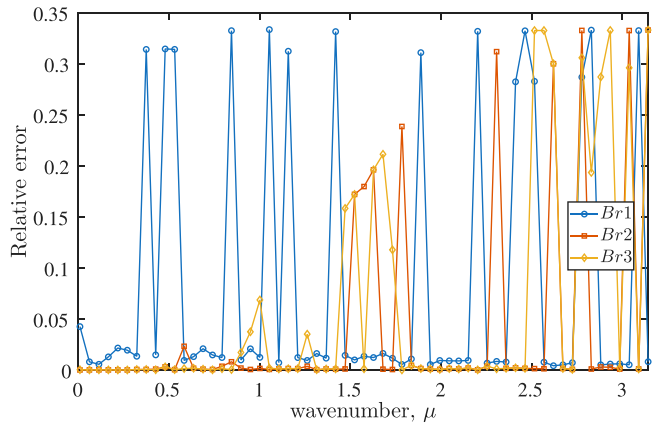

Fig. 20. Relative error $\left|\frac{\omega_{\mathrm{IM}}(\mu)-\omega_{\mathrm{HB}}(\mu)}{\omega_{\mathrm{HB}}(\mu)}\right|$ plotted against the wavenumber μ for all the three dispersion branches for a combination of mass ratios taken the same as for Fig. 19(a).

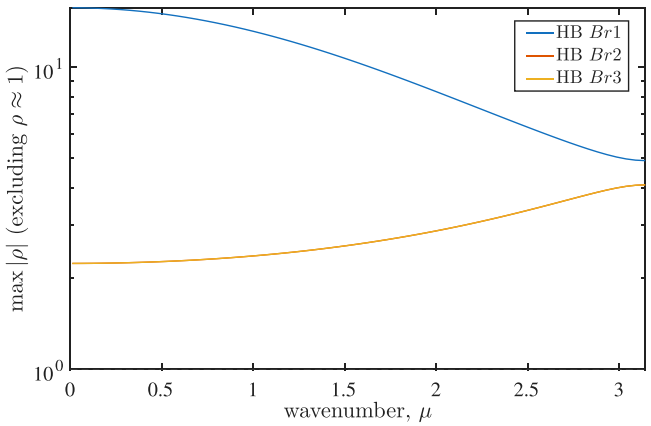

Fig. 21. Nonlinear Floquet stability of the harmonic balance (HB) periodic Bloch orbits for $r_1 = 0.1, r_2 = 1, r_a = 0.5$ (same parameter set as Fig. 19(a)), the quantity shown is the maximum modulus of the non-trivial Floquet multipliers, $\max_{\ell \neq triv} |\rho_\ell(\mu)|$, as a function of the Bloch wavenumber μ, Floquet multipliers are computed using a Hill/Floquet harmonic expansion retaining $N_{floq} = 5$ sideband harmonics, i.e. $2N_{floq} + 1 = 11$ Fourier sidebands in the perturbation ansatz, values above unity indicate linear instability of the corresponding periodic orbit.

minimal necessary criteria for chaos [42]. We do not notice aperiodicity in the time-domain over a significantly large time window. Since our system is deterministic in the sense that there is no random input, we go on to check the last necessary criterion for chaos i.e. positive Lyapunov exponent or in other words, a sensitive dependence on initial conditions. Two of the Lyapunov coefficients turned out to be greater than zero for the same system parameters. If the system is indeed chaotic, then the Nonlinear Normal Mode (NNM) solutions obtained through the convergence of the HB method would not be able to capture the actual physical behavior of a finite version of our model, because HB method inherently assumes periodic behavior in the steady state which contradicts the existence of chaos in any form. But, still the HB method can be a good framework to predict the system behavior in the non-chaotic or periodic regime and can efficiently reduce the computational cost of long time-domain simulations.

Nonlinear Floquet stability of the HB periodic Bloch orbits: To quantitatively assess whether the Harmonic Balance (HB) dispersion branches correspond to stable time-periodic Bloch waves, we compute the nonlinear Floquet multipliers ρ by linearizing the dynamics about each converged HB periodic orbit over one period (Hill/Floquet expansion with $N_{floq} = 5$ sideband harmonics and 9 samples of the perturbation Bloch phase ν) and plot $\max|\rho|$ with the wavenumber μ in Fig. 21. For the parameter set used in Fig. 19(a) ($r_1 = 0.1$, $r_2 = 1$, $r_a = 0.5$), the HB periodic solutions are found to be linearly unstable over the Brillouin zone. The maximum magnitude of the nontrivial multipliers, excluding the neutral multiplier $\rho \approx 1$ associated with time-shift invariance, reaches $\max_\mu |\rho| \approx 15.7$ for Branch 1 and $\max_\mu |\rho| \approx 4.08$ for Branches 2, 3. This provides a direct stability-based explanation consistent with the previously observed positive Lyapunov exponents. While HB can still compute the underlying periodic Bloch orbits, their loss of stability implies that time-domain trajectories may drift toward modulated or quasiperiodic responses in certain regimes, so the HB dispersion curves should be interpreted as continuations of periodic solutions rather than guaranteed stable propagating waves.

The other reason for this disparity between HB and IM results might be the root mean square (RMS) approximation to set the target amplitude for IM time-domain simulations. Our next approach in the future will be to find better methods of approximating the target amplitudes from the multi-harmonic HB steady state results. One more plausible reason for the discrepancy at few places could be due to the boundary effects which arises as an artifact of considering a finite chain for the purpose of numerical simulations. Though a damping layer has been used to minimize these boundary effects and the reference unit cell has been considered in the centre far away from the boundaries, in the strongly nonlinear regime, the wave profile might get distorted at some places due to reflections from the boundaries.

8. Conclusion and future work

An Amplitude-Locked, Inverse-method-Guided, multi-harmonic Nonlinear (ALIGN) framework, a comprehensive semi-analytical methodology for analyzing strongly nonlinear discrete periodic structures with non-integrable geometric nonlinearities has been presented. This method addresses three key challenges that limit existing approaches: (i) handling non-polynomial, algebraic forcing terms through time-domain collocation with complex-step differentiation, (ii) systematic validation via amplitude-locked time-domain simulations with RMS-targeted multi-harmonic initial conditions, and (iii) robust branch tracking through degeneracies using MAC-based feature matching on high-dimensional harmonic coefficient vectors. A summary of the methodology developed is shown in Fig. 22. The methodology was demonstrated on a bi-stable-inertial periodic chain exhibiting the full spectrum of computational difficulties: coupled horizontal-vertical dynamics, non-integrable square-root terms from geometric constraints (Eqs. (19)–(21)), and amplitude-dependent behavior requiring multiple harmonics ($N_h \geq 5$) for accurate representation. This successfully bridged weakly nonlinear (perturbation-based, Section 5) and strongly nonlinear (multi-harmonic balance, Section 6) regimes, with time-domain validation (Section 7) confirming amplitude-dependent dispersion predictions for a significant portion of the parameter space. The results obtained will have a significant impact on understanding the dynamical behavior and wave propagation characteristics of a fairly complex dynamical system both in its strongly and weakly nonlinear regime. Such a periodic lattice can be used for vibration suppression, vibration monitoring, vibration isolation and noise filtering among other applications. Key findings from the demonstration system include:

- Identification of critical parameter thresholds ($r_2 > 0.6$ keeping other mass ratios fixed, $r_a < 0.7$ keeping other mass ratios fixed) defining stability boundaries, consistent across weakly and strongly nonlinear regimes.
- Systematic bandgap manipulation through mass ratio variations (Tables 2, 3).

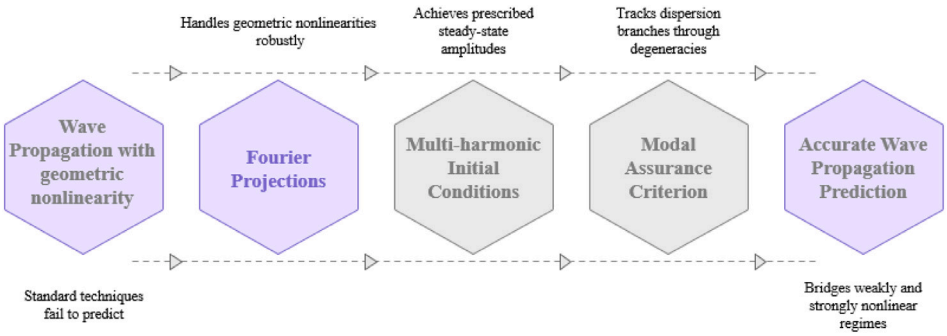

Fig. 22. A generalized framework for discrete nonlinear periodic structures.

- Modal redistribution in strongly nonlinear regime producing two dominant branches despite three DOFs per unit cell (explained in Section 6.2).
- Computational efficiency: The framework developed enables design space exploration significantly faster than direct time-domain simulation while maintaining accuracy for periodic solutions.

Key novel features of this work include:

- The main novelty of this work lies in the dynamical system considered itself. According to the best of the authors' knowledge, such a periodic lattice with geometric nonlinearity and inertial amplifiers has not been analyzed in the existing literature.
- In spite of being employed on this specific dynamic model, this framework is not restricted to the bi-stable-inertial system but applies to any discrete periodic structure with geometric, kinematic, or constraint-based nonlinearities expressible as algebraic functions. Examples include tensegrity metamaterials, origami-inspired structures, compliant mechanisms, granular chains with geometric contacts, and bio-inspired lattices with coupled rotational-translational DOFs.
- Systematic treatment of non-integrable nonlinearities via time-domain collocation with complex-step differentiation, generalizable to any algebraic geometric nonlinearity
- Amplitude-locked validation strategy with RMS-targeted multi-harmonic initial conditions enabling systematic time-domain verification across amplitude-wavenumber space. The amplitude-dependent dispersion curves and parametric maps (Figs. 6–19, Tables 2, 3) provide systematic design guidance for achieving desired bandgap characteristics. Designers can rapidly explore mass ratio, geometric angle, and amplitude parameter spaces without expensive time-domain simulations.
- Robust branch tracking through MAC-based feature matching preventing branch swapping through degeneracies and crossings.
- Unified framework spanning weakly to strongly nonlinear regimes with validated consistency between perturbation and harmonic balance approaches providing significant computational efficiency over direct time-domain simulation while maintaining accuracy for periodic solutions.

Future work on this system will focus on how the frequency varies systematically with the amplitude of the wave for a particular wavenumber in the strongly nonlinear regime. Also, there are two more parameters in the system other than the three mass ratios which are the angle of inclination of the inclined springs with the horizontal axis ϕ and the angle of inclination of the rigid links with the horizontal axis α when the system is in its initial unstressed/undeformed equilibrium configuration. Those two angles can be systematically varied to check how the dispersion profiles behave. As mentioned earlier, there were two critical values of r_2 and r_a for which the frequencies went to zero or became imaginary for all values of the wavenumber μ keeping other system parameters fixed. As a future step, these scenarios will be tried to be interpreted physically and investigated on how the mass ratios can be effectively tuned for vibration isolation and vibration suppression. The same methodology derived in this work can be extended to 2D/3D lattices which resemble more closely real-world periodic structures. This methodological framework can also be coupled with continuation methods to map stability boundaries and routes to chaos.

CRediT authorship contribution statement

A. Bhattacharyya: Writing – review & editing, Writing – original draft, Visualization, Validation, Supervision, Software, Resources, Project administration, Methodology, Investigation, Formal analysis, Data curation, Conceptualization. **S. Adhikari:** Writing – review & editing, Writing – original draft, Visualization, Validation, Supervision, Software, Resources, Project administration, Methodology, Investigation, Funding acquisition, Formal analysis, Data curation, Conceptualization.

Funding

The authors declare that no funds, grants, or other support was received during the preparation of this manuscript other than what is mentioned in the acknowledgments.

Declaration of competing interest

The authors declare that they have no known competing financial or non-financial interests or personal relationships that could have appeared to influence the work reported in this paper.

Acknowledgments

A. Bhattacharyya acknowledges the James Watt School of Engineering Ph.D. scholarship received from the University of Glasgow, UK.

Data availability

Data will be made available on request.

References

[1] X. Fang, W. Lacarbonara, L. Cheng, Advances in nonlinear acoustic/elastic metamaterials and metastructures, Nonlinear Dynam. (2024) 1–28.
[2] M.D. Fronk, L. Fang, P. Packo, M.J. Leamy, Elastic wave propagation in weakly nonlinear media and metamaterials: a review of recent developments, Nonlinear Dynam. 111 (12) (2023) 10709–10741.
[3] S. Hajarolasvadi, Mechanical Metamaterials for Wave Control: Effects Of Modularity and Nonlinearity (Ph.D. thesis), University of Illinois at Urbana-Champaign, 2021.

[4] M.I. Hussein, M.J. Leamy, M. Ruzzene, Dynamics of phononic materials and structures: Historical origins, recent progress, and future outlook, Appl. Mech. Rev. 66 (4) (2014) 040802.
[5] S.A. Cummer, J. Christensen, A. Alù, Controlling sound with acoustic metamaterials, Nat. Rev. Mater. 1 (2016) 16001.
[6] K. Bertoldi, V.V.J. Christensen, M. van Hecke, Flexible mechanical metamaterials, Nat. Rev. Mater. 2 (2017) 17066.
[7] P.A. Deymier (Ed.), Acoustic Metamaterials and Phononic Crystals, Springer, 2013.
[8] L. Brillouin, Wave Propagation in Periodic Structures, second ed., Dover, 1953.
[9] D.J. Mead, Wave propagation in continuous periodic structures: research contributions from southampton, 1964–1974, J. Sound Vib. 40 (1) (1975) 1–18.
[10] Z. Chen, W. Zhou, C.W. Lim, Active control for acoustic wave propagation in nonlinear diatomic acoustic metamaterials, Int. J. Non-Linear Mech. 125 (2020) 103535.
[11] R.K. Narisetti, Wave Propagation in Nonlinear Periodic Structures, Georgia Institute of Technology, 2010.
[12] F.E. Udwadia, H. Mylapilli, Energy control of inhomogeneous nonlinear lattices, Proc. R. Soc. A: Math. Phys. Eng. Sci. 471 (2176) (2015) 20140694.
[13] N. Contreras, X. Zhang, H. Hao, F. Hernández, Application of elastic metamaterials/meta-structures in civil engineering: A review, Compos. Struct. 327 (2024) 117663.
[14] A. Banerjee, S. Adhikari, M.I. Hussein, Inertial amplification band-gap generation by coupling a levered mass with a locally resonant mass, Int. J. Mech. Sci. 207 (2021) 106630.
[15] S. Chowdhury, A. Banerjee, S. Adhikari, The exact closed-form expressions for optimum inertial amplifier coupled nonlinear friction bearing isolators, in: International Conference on Nonlinear Dynamics and Applications, 2023, pp. 165–176.
[16] S. Chowdhury, A. Banerjee, S. Adhikari, The nonlinear negative stiffness inertial amplifier base isolators for dynamic systems, Mech. Based Des. Struct. Mach. 52 (11) (2024) 8430–8469.
[17] S. Chowdhury, A. Banerjee, S. Adhikari, Enhancing seismic resilience of structures through optimally designed nonlinear negative stiffness base isolators: Exact closed-form expressions, Nonlinear Dynam. 112 (18) (2024) 15833–15856.
[18] S.R. Panigrahi, Dynamics of Nonlinear Snap–Through Chains with Application to Energy Harvesting and Wave Propagation, Michigan State University, 2014.
[19] N. Nadkarni, C. Daraio, D.M. Kochmann, Dynamics of periodic mechanical structures containing bistable elastic elements: From elastic to solitary wave propagation, Phys. Rev. E 90 (2) (2014) 023204.
[20] J.G. Cui, M.Q. Niu, L.Q. Chen, T. Yang, Asymmetric propagation of acoustic waves in a conical granular chain, Commun. Nonlinear Sci. Numer. Simul. 116 (2023) 106885.
[21] H. Jalali, P. Rizzo, A. Nasrollahi, Asymmetric propagation of low-frequency acoustic waves in a granular chain using asymmetric intruders, J. Appl. Phys. 126 (7) (2019).
[22] R. Yazbeck, S. El-Borgi, J.G. Boyd, M. Chen, D.C. Lagoudas, Non-dimensional linear analysis of one-dimensional wave propagation in tensegrity structures, Compos. Struct. 353 (2025) 118694.
[23] D.R. Santo, E. Deckers, P.J.P. Goncalves, L.P.R. de Oliveira, Improving the vibration control performance of metamaterial structures by the inclusion of nonlinear local resonators, in: XLIV Ibero-Latin American Congress on Computational Methods in Engineering, Vol. 5, 2023.
[24] K.L. Manktelow, Dispersion Analysis of Nonlinear Periodic Structures (Ph.D. thesis), Georgia Institute of Technology, 2013.
[25] K.L. Manktelow, M.J. Leamy, M. Ruzzene, Weakly nonlinear wave interactions in multi-degree of freedom periodic structures, Wave Motion 51 (6) (2014) 886–904.
[26] K.L. Manktelow, M. Ruzzene, M.J. Leamy, Wave propagation in nonlinear lattice materials, Dyn. Lattice Mater. (2017) 107–137.
[27] M.D. Fronk, M.J. Leamy, Higher-order dispersion, stability, and waveform invariance in nonlinear monoatomic and diatomic systems, J. Vib. Acoust. 139 (5) (2017) 051003.
[28] A.H. Nayfeh, Introduction to Perturbation Techniques, Wiley, 1993.
[29] A.H. Nayfeh, D.T. Mook, Nonlinear Oscillations, Wiley, 1979.
[30] C.M. Cheng, Z.K. Peng, W.M. Zhang, G. Meng, Analysis of locally nonlinear two dimensional periodic structures using NOFRFs, in: Vibration Engineering and Technology of Machinery: Proceedings of VETOMAC X 2014, Held At the University of Manchester, UK, September 9-11, 2014, 2014, pp. 811–823.
[31] C.M. Cheng, Z.K. Peng, X.J. Dong, W.M. Zhang, G. Meng, Locating non-linear components in two dimensional periodic structures based on NOFRFs, Int. J. Non-Linear Mech. 67 (2014) 198–208.
[32] M.P. Magalhães, et al., Análise da formação de Band Gaps em estruturas periódicas utilizando o método do elemento espectral, 2023.
[33] X. Liu, G. Cai, K.W. Wang, Dispersion analysis of a two-dimensional metastable metastructure considering damping and nonlinear effects, J. Appl. Phys. 129 (11) (2021).
[34] H. Reda, K. Elnady, J.F. Ganghoffer, H. Lakiss, Wave propagation in pre-deformed periodic network materials based on large strains homogenization, Compos. Struct. 184 (2018) 860–871.
[35] A. Parsa, J. Bagrow, C.S. O'Hern, R. Kramer-Bottiglio, J. Bongard, Data-driven modeling of granular chains with modern koopman theory, 2024, arXiv preprint arXiv:2411.15142.
[36] G. Kerschen, M. Peeters, J.C. Golinval, A.F. Vakakis, Nonlinear normal modes, Part I: A useful framework for the structural dynamicist, Mech. Syst. Signal Process. 23 (1) (2009) 170–194.
[37] G. Haller, S. Ponsioen, Nonlinear normal modes and spectral submanifolds: Existence, uniqueness and use in model reduction, J. Nonlinear Sci. 26 (4) (2016) 909–966.
[38] T. Breunung, G. Haller, Explicit backbone curves from spectral submanifolds of forced-damped nonlinear mechanical systems, Proc. R. Soc. A 474 (2213) (2018) 20180083.
[39] S. Ponsioen, T. Pedergnana, G. Haller, Model reduction to spectral submanifolds and forced-response calculation in high-dimensional mechanical systems, J. Sound Vib. 488 (2020) 115640.
[40] S. Chowdhury, A. Banerjee, The nonlinear dynamic analysis of optimum nonlinear inertial amplifier base isolators for vibration isolation, Nonlinear Dynam. 111 (14) (2023) 12749–12786.
[41] S. Flach, A.V. Gorbach, Discrete breathers—advances in theory and applications, Phys. Rep. 467 (1–3) (2008) 1–116.
[42] S.H. Strogatz, Nonlinear Dynamics and Chaos, Perseus Books Publishing, 1994.
[43] B. Yan, N. Yu, H. Ma, C. Wu, A theory for bistable vibration isolators, Mech. Syst. Signal Process. 167 (2022) 108507.
[44] S.S. Rao, Vibration of Continuous Systems, John Wiley & Sons, 2019.
[45] M.A. Campana, M. Ouisse, E. Sadoulet-Reboul, M. Ruzzene, S. Neild, F. Scarpa, Impact of non-linear resonators in periodic structures using a perturbation approach, Mech. Syst. Signal Process. 135 (2020) 106408.